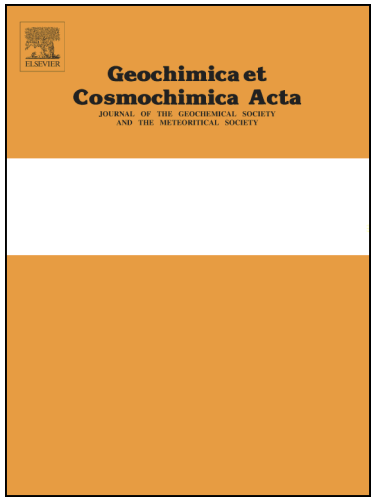

Solubility of water in lunar basalt at low pH_2O

M.E. Newcombe, A. Brett, J.R. Beckett, M.B. Baker, S. Newman, Y. Guan, J.M. Eiler, E.M. Stolper

PII: S0016-7037(16)30735-9
DOI: http://dx.doi.org/10.1016/j.gca.2016.12.026
Reference: GCA 10078

To appear in: *Geochimica et Cosmochimica Acta*

Received Date: 22 June 2016
Revised Date: 10 December 2016
Accepted Date: 19 December 2016

Please cite this article as: Newcombe, M.E., Brett, A., Beckett, J.R., Baker, M.B., Newman, S., Guan, Y., Eiler, J.M., Stolper, E.M., Solubility of water in lunar basalt at low pH_2O, *Geochimica et Cosmochimica Acta* (2016), doi: http://dx.doi.org/10.1016/j.gca.2016.12.026

SOLUBILITY OF WATER IN LUNAR BASALT AT LOW pH_2O

M.E. Newcombe[a,*], A. Brett[b], J.R. Beckett[a], M.B. Baker[a], S. Newman[a], Y. Guan[a], J.M. Eiler[a], and E.M. Stolper[a]

[a] Division of Geological and Planetary Sciences, California Institute of Technology, Pasadena, CA 91125, USA

[b] Imperial College London, South Kensington Campus, London SW7 2AZ, UK

*Corresponding author, now at Lamont-Doherty Earth Observatory of Columbia University, Palisades, NY 10964, USA; Email: newcombe@ldeo.columbia.edu

Abstract

We report the solubility of water in Apollo 15 basaltic 'Yellow Glass' and an iron-free basaltic analog composition at 1 atm and 1350 °C. We equilibrated melts in a 1-atm furnace with flowing H_2/CO_2 gas mixtures that spanned ~8 orders of magnitude in fO_2 (from three orders of magnitude more reducing than the iron-wüstite buffer, IW−3.0, to IW+4.8) and ~4 orders of magnitude in pH_2/pH_2O (from 0.003 to 24). Based on Fourier transform infrared spectroscopy (FTIR), our quenched experimental glasses contain 69–425 ppm total water (by weight). Our results demonstrate that under the conditions of our experiments: (1) hydroxyl is the only H-bearing species detected by FTIR; (2) the solubility of water is proportional to the square root of pH_2O in the furnace atmosphere and is independent of fO_2 and pH_2/pH_2O; (3) the solubility of water is very similar in both melt compositions; (4) the concentration of H_2 in our iron-free experiments is <~4 ppm, even at oxygen fugacities as low as IW−2.3 and pH_2/pH_2O as high as 11; (5) Secondary ion mass spectrometry (SIMS) analyses of water in iron-rich glasses equilibrated under variable fO_2 conditions may be strongly influenced by matrix effects, even when the concentration of water in the glasses is low; and (6) Our results can be used to constrain the entrapment pressure of lunar melt inclusions and the partial pressures of water and molecular hydrogen in the carrier gas of the lunar pyroclastic glass beads. We find that the most water-rich melt inclusion of Hauri et al. (2011) would be in equilibrium with a vapor with pH_2O ~3 bar and pH_2 ~8 bar. We constrain the partial pressures of water and molecular hydrogen in the carrier gas of the lunar pyroclastic glass beads to be 0.0005 bar and 0.0011 bar respectively. We calculate that batch degassing of lunar magmas containing initial volatile contents of 1200 ppm H_2O (dissolved primarily as hydroxyl) and 4–64 ppm C would produce enough vapor to reach the critical vapor volume fraction thought to be required for magma

fragmentation (~65–75 vol. %) at a total pressure of ~5 bar (corresponding to a depth beneath the lunar surface of ~120 m). At a fragmentation pressure of ~5 bar, the calculated vapor composition is dominated by H_2, supporting the hypothesis that H_2, rather than CO, was the primary propellant of the lunar fire fountain eruptions. The results of our batch degassing model suggest that initial melt compositions with >~200 ppm C would be required for the vapor composition to be dominated by CO rather than H_2 at 65–75 % vesicularity.

1. Introduction

Recent detections of dissolved water in lunar volcanic glasses and melt inclusions (Saal et al. 2008; Hauri et al. 2011; Saal et al. 2013; Chen et al. 2015; Wetzel et al. 2015), lunar apatites (Boyce et al. 2010; McCubbin et al. 2010; Greenwood et al. 2011; Tartèse et al. 2014), and plagioclase from lunar highland anorthosites (Hui et al. 2013) have led to a reevaluation of what has appeared for decades to be one of the definitive results of the study of lunar samples: i.e., that the sources of lunar magmas—and, by inference, the entire Moon—are much poorer in water than the Earth; indeed the Moon had been described as "bone dry" (Newsom and Taylor 1989). In particular, direct measurements of water in incompletely degassed, primitive lunar glasses made in several laboratories have shown that water concentrations are similar to those observed in magmas from Earth's depleted upper mantle (Saal et al. 2008; Chen et al. 2015; Hauri et al. 2015; Wetzel et al. 2015) and that the isotopic composition of this water is approximately chondritic (Friedman et al. 1974; Saal et al. 2013; Barnes et al. 2014; Füri et al. 2014; Tartèse et al. 2014). Although these results and their generality to the Moon as a whole are not universally accepted (Sharp et al. 2010; Greenwood et al. 2011; Albarède et al. 2015), these observations have been interpreted as signifying a common origin for terrestrial and lunar water (Saal et al. 2013). The incorporation of water into the Moon in concentrations similar to those of the Earth is seemingly at odds with the widely held view of the origin of the Moon as the result of an impact between the early Earth and a Mars-sized impactor (e.g., Canup and Asphaug 2001; Pahlevan and Stevenson 2007). Thus, the identification of unexpectedly "wet" lunar glasses (and other phases) has led to renewed interest in the formation and evolution of the Moon (e.g., Nakajima and Stevenson 2014; Canup et al. 2015; Hauri et al. 2015).

In addition to its importance for understanding the origin of the Moon, the unexpected water concentrations observed or inferred for lunar magmas also have implications for our understanding of magma generation, migration, and eruption on the Moon. However, full exploration of these implications requires knowledge of phase equilibria (e.g., water solubility) and transport properties (e.g., the diffusivity of water) for molten lunar basalts under conditions relevant to the near surface of the Moon. Although extensively studied for terrestrial melt compositions and conditions (e.g., Stolper 1982a; Zhang

and Stolper 1991; McMillan 1994; Dixon et al. 1995; Moore et al. 1998; Berndt et al. 2002; Benne and Behrens 2003; Zhang et al. 2007; Behrens et al. 2009; Lesne et al. 2010; Morizet et al. 2010; Persikov et al. 2010; Zhang and Ni 2010; Iacono-Marziano et al. 2012; Shishkina et al. 2014), water solubility and diffusion have not been studied for melts approaching the high iron contents of lunar magmas, and at the low fO_2's and relatively low pH_2O conditions of the Moon. Another source of uncertainty in lunar volcanic degassing models is the role of molecular hydrogen (Elkins-Tanton and Grove 2011; Zhang 2011; Hirschmann et al. 2012; Sharp et al. 2013; McCubbin et al. 2015), with some authors suggesting that molecular hydrogen may be the main propellant of the lunar fire-fountain eruptions (Sharp et al. 2013; McCubbin et al. 2015), while other authors argue that the low solubility of molecular hydrogen in silicate melts at low pressures and low total H contents precludes a significant role for molecular hydrogen dissolution under low-pressure near-surface lunar conditions (Hirschmann et al. 2012).

The goal of this work is to measure the solubility of water in a lunar volcanic glass composition and in a simplified basaltic composition under the low pH_2O and low fO_2 conditions thought to be prevalent during lunar volcanic eruptions (Sato 1976; Wadhwa 2008). We conducted water solubility experiments by equilibrating melts with H_2O-bearing vapor at 1 atm over a range of fO_2 and pH_2/pH_2O and then measuring via Fourier transform infrared spectroscopy (FTIR) and secondary ion mass spectrometry (SIMS) the concentrations of water or hydrogen in glasses quenched from these melts. We compare our results to the few published studies of water solubility in basaltic melts at low pressures and to extrapolations to low pressures of existing models of water solubility in silicate melts. We then use our data to place constraints on the concentration of molecular hydrogen dissolved in silicate melts equilibrated under highly reducing conditions (i.e., at oxygen fugacities as low as three log units below the iron-wüstite buffer), on the depths of entrapment of the lunar melt inclusions (e.g., Hauri et al. 2011), and on the composition of the carrier gas associated with lunar pyroclastic glass beads (Saal et al. 2008; Wetzel et al. 2015).

2. Background

2.1. Speciation of water in silicate melts

A silicate melt in equilibrium with a water-bearing vapor dissolves water as both water molecules (H_2O_{mol}) and hydroxyl groups (OH) according to the following chemical reactions (Stolper 1982a):

$$H_2O^{vapor} \leftrightarrow H_2O^{melt}_{mol} \quad (1)$$

$$H_2O^{melt}_{mol} + O^{0,melt} \leftrightarrow 2OH^{melt} \quad (2)$$

In reaction (2), $O^{0,melt}$ could be a bridging oxygen (i.e., an oxygen bridging two tetrahedrally coordinated, network-forming cations), a non-bridging oxygen in an aluminosilicate tetrahedron, or a "free" oxygen; and OH^{melt} represents a hydroxyl group bonded to an aluminosilicate polymer (Behrens and Nowak 1997; Kohn 2000) or an alkali or alkaline-earth cation (Le Losq et al. 2015). Combining reactions (1) and (2) yields the reaction $H_2O_{mol}^{vapor} + O^{0,melt} \leftrightarrow 2OH^{melt}$, which is governed by an equilibrium constant K_{eq} (Stolper 1982a) that can be approximated by

$$K_{eq} \cong \frac{[OH^{melt}]^2}{fH_2O^{vapor}[O^{0,melt}]} \ , \qquad (3)$$

where square brackets indicate mole fractions calculated on a single oxygen basis (e.g., Stolper 1982a; Zhang et al. 1991; Zhang et al. 2007), and fH_2O^{vapor} is the fugacity of water in the vapor. Note that the calculation of mole fractions on a single oxygen basis requires that $[O^{0,melt}] + [OH^{melt}] + [H_2O_{mol}^{melt}] = 1$ and that the mole fraction of *total* water ($[H_2O_{tot}]$) dissolved in the melt as both hydroxyl groups ($[OH]$) and molecular water ($[H_2O_{mol}]$) is equal to $[H_2O_{mol}] + [OH]/2$ (Stolper 1982a; Zhang 1999).

Concentrations of water dissolved as molecular water and as hydroxyl have been measured by FTIR in glasses quenched from melts for several bulk compositions across a wide range of total water concentrations, where total water refers to the sum of the amounts of water dissolved as molecular water and as hydroxyl (Stolper 1982b; Silver and Stolper 1989; Silver et al. 1990; Dixon et al. 1995). Results of these studies suggest that water dissolved as hydroxyl is likely to be dominant at the low total water concentrations observed in lunar glasses (Fig. 1). With increasing water content, the proportion of water dissolved as molecular water increases such that the concentrations of water dissolved as hydroxyl and as molecular water are comparable at total water contents of a few weight percent. With further increases in total water content, molecular water becomes the dominant species and the hydroxyl content levels off or may even decrease. The observed concentrations of hydroxyl and molecular water at different total water concentrations are well described by equations (1)–(3), although the appropriate solution model to describe the mixing of OH, H_2O_{mol} and O^0 in the melt is still not completely resolved (Silver and Stolper 1989; Silver et al. 1990; Dixon et al. 1995; Chertkova and Yamashita 2015), and the effect of quenching on the speciation of water in glasses versus high temperature melts is still debated (Stolper 1989; Dingwell and Webb 1990; Silver et al. 1990; Dixon et al. 1995; Sowerby and Keppler 1999; Withers et al. 1999; Nowak and Behrens 2001; Lesne et al. 2010).

The solubility of water in silicate melts is known to be strongly dependent on pressure (e.g., Goranson 1931; Hamilton et al. 1964; Orlova 1964; McMillan 1994; Dixon et al. 1995; Liu et al. 2005; Moore 2008; Lesne et al. 2010; Shishkina et al. 2014). At sufficiently low pressures, only small quantities of water dissolve in the melt; consequently, because the reaction of molecular water with oxygen in the

melt to produce hydroxyl groups causes a negligible reduction of the large number of reactive oxygens in the melt (whether bridging, non-bridging, or free), it can be assumed that $[O^{0,melt}]$ is approximately constant. Equation (3) thus can be reduced to:

$$[OH^{melt}] \propto \sqrt{f H_2O^{vapor}} \ . \quad (4)$$

Moreover, at the low total water contents of lunar magmas (<1,500 ppm), less than ~50 ppm (by weight) of the total dissolved water is expected to be dissolved as water molecules (i.e., > 97% of the dissolved water is present as hydroxyl groups; Fig. 1), and thus the mole fraction of hydroxyl in the melt (calculated as total H_2O using the relationship $[H_2O^{melt}_{tot}] = [OH^{melt}]/2$) is essentially identical to the total concentration of dissolved water.

The relationship expressed in equation (4) is known as Sieverts' law in metallurgy, which describes the dissolution of diatomic gases in metals (Sieverts 1929). The solubility of water in glasses at ambient pressure has long been of interest to researchers in the glass industry, and several studies have demonstrated the applicability of equation (4) to a range of synthetic silicate glass and melt compositions (Tomlinson 1956; Kurkjian and Russell 1958; Moulson and Roberts 1961; McMillan 1994). However, few studies of water solubility in natural silicate melt and glass compositions have been conducted at a total pressure of ~1 atm (Friedman et al. 1963; Baker and Grove 1985; Liu et al. 2005), so current understanding of water solubility in natural silicate melts at low pressure is largely confined to the extrapolation of results of water solubility experiments conducted at higher pressures and water contents. Several models and empirical parameterizations of water solubility in silicate melts have been developed, some of which recover the proportionality connecting water concentration and $fH_2O^{0.5}$ at low pressures given by equation (4) (Stolper 1982a; Silver and Stolper 1989; Dixon et al. 1995; Pineau et al. 1998; Newman and Lowenstern 2002; Liu et al. 2005) and others of which assume general power law relationships between water concentration and fH_2O, some of which are inconsistent with Sieverts' law and equation (4) (Moore et al. 1998; Papale et al. 2006; Lesne et al. 2010; Duan 2014; Shishkina et al. 2014; Burgisser et al. 2015). One aim of this study is to test the applicability of equation (4) to two geologically relevant silicate melt compositions at a total pressure of 1 atm.

2.2. The potential role of other H-bearing species in lunar melts under reducing conditions

In addition to molecular water and hydroxyl, silicate melts can also dissolve other H-bearing species, such as molecular hydrogen (Hirschmann et al. 2012; Armstrong et al. 2015), NH-bearing species (Armstrong et al. 2015), and hydrocarbons such as methane (Taylor and Green 1987; Mysen et al. 2009; Mysen and Yamashita 2010; Mysen et al. 2011; Ardia et al. 2013; Armstrong et al. 2015). The H-C-O vapor in our experiments contains negligible N, and, under the conditions of our experiments, CH_4 can also be neglected (Deines et al. 1974; Zhang and Duan 2009). However, our most reducing experimental

glasses were equilibrated with atmospheres containing >90% H_2, so the possible dissolution of H as molecular hydrogen must be considered.

Following a treatment similar to that described above for water, it can be shown that the solubility of H_2 in a silicate melt in equilibrium with an H-bearing vapor is expected to be proportional to the fugacity of H_2 in the vapor (Zhang and Ni 2010; Hirschmann et al. 2012):

$$[H_2^{melt}] \propto f H_2 \ . \quad (5)$$

Several authors have suggested that H_2 dissolution could be important in the eruptive products of planetary bodies, including the Moon, that are more reduced than the Earth (Zhang and Ni 2010; Elkins-Tanton and Grove 2011; Zhang 2011; Sharp et al. 2013; McCubbin et al. 2015). However, extrapolation (from 0.7–3 GPa) to low pressures of recent experimental data on the solubility of H_2 in basaltic melts (Hirschmann et al. 2012) suggests that basaltic melt in equilibrium with 1 atm of pure H_2 likely contains only ~0.4 ppm (by weight) dissolved molecular hydrogen.

Our experiments offer the opportunity to explore the importance of H_2 dissolution in lunar basalt for water solubility: i.e., we have equilibrated lunar basaltic melts over a significant range of fH_2/fH_2O ratios (0.003–24), and the quenched melts from these experiments have been analyzed by FTIR and SIMS. FTIR can be used to quantify the concentrations of individual H-bearing species in silicate melts (Stolper 1982b; Newman et al. 1986), including H_2 if present in concentrations greater than ~700 ppm (Hirschmann et al. 2012; Ardia et al. 2013), whereas SIMS measures bulk H contents. By comparing concentrations of H-bearing species measured by both techniques in experiments with varying fH_2/fH_2O, it is possible to set limits on the amount of dissolved H_2 and thereby to assess the importance of dissolved H_2 in melts at the low pressures relevant to the near-surface lunar environment.

3. Methods

We equilibrated a synthetic Apollo 15 'Yellow Glass' (Delano 1980; Delano 1986), which is thought to have been produced by a basaltic fire fountain eruption (Fogel and Rutherford 1995; Rutherford and Papale 2009), and an iron-free basaltic analog close to the 1-atm eutectic composition on the anorthite-diopside join with flowing H_2-CO_2 gas mixtures at 1350 °C and 1 atm total pressure. [Note that at a total pressure, P_{tot}, of 1 atm and magmatic temperatures, the behavior of H_2-CO_2 gas mixtures is so close to ideal that the fugacity of each species in the vapor is essentially equal to its partial pressure (e.g., Jakobsson and Oskarsson 1994; Duan 2014), which is in turn equal to the mole fraction of that species in the vapor (e.g., Deines et al. 1974). The assumption of gas ideality will be applied for the remainder of this study, and fugacity and partial pressure will be used interchangeably.] The ratio of the partial pressure of hydrogen to the partial pressure of water (pH_2/pH_2O) in the resultant vapor was varied

from 0.003 to 24, resulting in variation of pO_2 from ~10^{-13} to ~10^{-5} (IW−3.0 to IW+4.8). Concentrations of dissolved water in the quenched glasses were measured by FTIR and SIMS. In the following subsections, we provide details of synthesis procedures and of experimental and analytical techniques.

3.1. Starting materials

Synthetic Apollo 15 'Yellow Glass' (hereafter referred to as 'lunar glass' and abbreviated LG) was made by combining reagent-grade powdered oxides and carbonates. Oxide and carbonate powders were weighed on a balance with a precision of 0.1 mg after baking at appropriate temperatures in order to minimize adsorbed water. The resultant powder was mixed under ethanol in an alumina mortar for ~4 hours, decarbonated at 800 °C, and then placed in a shallow alumina boat and reduced at 900 °C in a horizontal Lindberg furnace. A mixture of H_2 and CO_2 corresponding to an oxygen fugacity of IW+1 was flowed through a platinum mesh in order to catalyze the reaction between H_2 and CO_2 (Beckett and Mendybaev 1997) and this gas mixture was then allowed to flow over the powder. After ~1 hour, the furnace was switched off, and the alumina boat was slowly pulled towards the cool part of the furnace (whilst maintaining a seal to prevent oxidation of the powder). The efficacy of the powder reduction could be assessed by the change in color of the powder from red to gray (caused by the reduction of Fe^{3+} to Fe^{2+} in the powder). Following this step, the powder was pressed into pellets measuring ~1 cm in diameter, and chips of these pellets weighing ~20–70 mg were used as starting material for the LG experiments.

Mixtures of anorthite and diopside glasses corresponding to compositions close to the 1-atm eutectic composition on the anorthite-diopside join (~$An_{36}Di_{64}$, abbreviated AD) were prepared by weighing out anorthite and diopside glasses (provided by G.J. Fine of Corning Glass). Two different batches of this composition were used: The first batch ("AD Batch 1" in Table 1) was provided by the Caltech shock wave laboratory and was previously used by Asimow and Ahrens (2010). As described by Asimow and Ahrens (2010), anorthite and diopside glass chips were powdered in a percussion mortar, dried at 110 °C prior to weighing, and combined under ethanol in an agate mortar for 30 minutes. The resultant mixed powder was fused under vacuum for 24 hours at 1400 °C, quenched in air, reground in an agate mortar under ethanol, and fused a second time. This starting material was then annealed at 500 °C overnight. A second batch of ~$An_{36}Di_{64}$ glass ("AD Batch 3" in Table 1) was purpose-made for this study after the first batch was used up. For this second batch, anorthite and diopside glasses from Corning Glass (~1 mm chips and glass wool) were crushed, dried, weighed, and mixed together under ethanol in an alumina mortar for ~4 hours. The resultant glass powder was placed in a platinum crucible and held in a 1-atm Deltech vertical furnace under air at 1398 °C for 16 hours. The anorthite-diopside (AD) melt was quenched to a glass by pulling the platinum crucible out of the top of the furnace and plunging it into a beaker of distilled water. The AD glass was removed from the platinum crucible and broken into small

chips with the use of a Plattner mortar. Potential contamination of the glass by small flakes of metal from the mortar was minimized by passing a magnet over the glass chips. The compositions of LG and AD glasses are reported in Table 1. For the AD experiments, the batch number (i.e., Batch 1 or Batch 3) used as starting material for each experiment is indicated in Table 2.

3.2. Experimental methods

Chips of AD glass and LG pressed-powder pellets were balanced on wire loops. Once molten, the samples formed beads with diameters of ~3 mm that clung to the wire loops by surface tension. One to two loops were run in a given experiment. Platinum wire loops were used for all AD experiments. Most of the LG experiments utilized 0.25 mm diameter rhenium wire loops (99.97% Re), so as to reduce the loss of iron from the melt to the metal (via the reaction $FeO^{melt} \leftrightarrow Fe^{metal} + 0.5O_2$) over the course of the experiment (Borisov and Jones 1999). However, rhenium volatilizes at oxygen fugacities above ~QFM (Borisov and Jones 1999) at the temperatures of our experiments, so a thin platinum wire loop (0.008 inch diameter) was used for the most oxidizing LG experiment (LG35). We used molybdenum wire for the two most reducing experiments (LG6 at IW−2.2 and LG7 at IW−3.0), because under such reducing conditions, molybdenum is more effective than rhenium for avoiding iron loss (Hess et al. 1975). As shown in Fig. 2, the use of rhenium wire loops proved to be successful at minimizing iron loss from experiments for oxygen fugacities above IW. Experiments LG40 and LG7 were reducing enough that they precipitated iron-rich metal blebs and this left the residual melt significantly depleted in iron. As described above, the most oxidizing experiment (LG35) was hung from a thin platinum wire loop, but this experiment experienced little to no iron loss into the platinum (Fig. 2). Compositions of a subset of our experimental glasses are provided in the supplement.

Flowing mixtures of H_2 and CO_2 gases were used to control the oxygen fugacity and the partial pressures of H_2, CO_2, H_2O, and CO in the hotspot of a 1-atm furnace. At any given temperature, the initial H_2/CO_2 ratio of the inflowing gas mixture (R), fixes its equilibrium pH_2O, pO_2, pCO_2, and pH_2 at high temperatures (see Fig. 3 and Deines et al. 1974). With decreasing R, pH_2 decreases monotonically, pCO_2 increases monotonically, and pH_2O is maximized at R=1, i.e. at IW+0.3 (Fig. 3). Therefore, for any value of pH_2O (except at the R=1 maximum), there are two possible values of pH_2 and pO_2. We will exploit this feature of the system to determine the dependence (if any) of water solubility on pH_2 and pO_2.

All experiments were conducted at 1350 °C. Temperature measurements were made using a type-S thermocouple and the oxygen fugacity was measured using an yttria-stabilized zirconia oxygen sensor (SIRO2; Ceramic Oxide Fabricators, Eaglehawk, Australia). The accuracy of the sensor was checked at the IW buffer and was found to be within 0.15 log units of the calibrations of Huebner (1971) and O'Neill and Pownceby (1993). During our early experiments, needle dials connected to analog flow meters were used to control and monitor the flow rates of H_2 and CO_2. Some of these experiments (AD12, AD13,

LG1, LG2, LG3, LG4, LG5, LG6 and LG7) were conducted with an oxygen sensor that was later discovered to be faulty, but we were able to recover the oxygen fugacity of these compromised experiments by returning to the needle dial and flow rate settings recorded for the experiments and re-measuring the oxygen fugacity of the gas mixture using a new oxygen sensor. We also repeated some of these experiments to confirm the accuracy of this correction technique. In later runs (AD23, AD25, AD26, LG35, LG38, LG39 and LG40), the flow rates of H_2 and CO_2 were set using Sierra SmartTrak M100 and Sierra MicroTrak M101 mass flow controllers. For these experiments, the oxygen fugacity measured by the oxygen sensor and that calculated from the known flow rates agreed to within 0.1 log units and no systematic offset was observed.

At the beginning of each AD experiment, glass chips balanced on platinum wire loops were placed directly into the hotspot of the furnace under air or N_2 gas. The gas mixture was then changed to a mixture of H_2 and CO_2 previously determined to produce the desired fO_2 and the sample allowed to equilibrate for 3–21 hours before being drop-quenched into deionized water. This procedure could not be used for LG experiments conducted using rhenium wire because the wire was prone to catastrophic volatilization when it came into contact with air in the furnace hotspot. At the beginning of each LG experiment, the furnace was flushed with N_2 gas, and the sample was placed above the hotspot at a temperature of a few hundred degrees centigrade. Once the furnace was sealed, the N_2 gas was turned off and the desired H_2/CO_2 gas mixture for that experiment was then flushed through the furnace for ~10 minutes. The sample was then lowered into the hotspot and allowed to equilibrate with the gas mixture for 4–47 hours before being drop-quenched in deionized water. The reproducibility of water concentrations measured in pairs of experiments conducted at similar pH_2/pH_2O conditions but for different durations (e.g., AD1b and AD13; see Table 2) demonstrates that run times were sufficient for the attainment of equilibrium. AD and LG experiments that stayed intact during the quench were cut through their centers on a Unipress Precision Wire Saw and one half was doubly polished to produce a wafer of glass with a thickness of a few hundred microns suitable for FTIR analysis, while the other half was saved for analysis by SIMS. For those experiments that broke on quenching, a few large fragments relatively free of cracks were doubly polished for analysis by FTIR and other fragments were singly polished for analysis by SIMS. Results of these analyses are listed in Table 2.

3.3. Measuring the concentration of dissolved water by FTIR

Experimental glasses were analyzed by transmission FTIR using a Nicolet Magna-IR 860 FTIR spectrometer equipped with a Nicolet Continuμm IR microscope, a CaF_2 beamsplitter, and a MCT/A detector cooled with liquid N_2. Spectra were collected using a ~25×80 μm aperture across a wavenumber range of 1300–7000 cm^{-1} with a resolution of 4 cm^{-1}, and 2048 scans were averaged for each analysis.

Because of the low concentrations of water in our samples, we used the 3550 cm^{-1} absorption band (Fig. 4) to determine total dissolved water contents. This band is due to fundamental vibrational modes in both hydroxyl and molecular water (Stolper 1982b; Newman et al. 1986; Dixon et al. 1995); i.e., it does not distinguish between these two dissolved species and gives only a measurement of total water. The concentration of water was calculated using the Beer-Lambert law (Stolper 1982b):

$$C_{water} = \frac{100 \times Abs_{3550} \times 18.015}{d \times \rho \times \varepsilon_{3550}} \quad (6)$$

In this expression, C_{water} is the concentration of water in wt% (i.e., the amount of water that would be measured if all of the molecular water and hydroxyl were removed as H_2O on heating), Abs_{3550} is the background-corrected peak height of the absorbance peak at ~3550 cm^{-1}; 18.015 is the molecular weight of H_2O in atomic mass units; d is the thickness of the glass wafer in cm; ρ is the density of the glass in g/l; and ε_{3550} is the molar absorptivity of water at 3550 cm^{-1} in $l \cdot mol^{-1} \cdot cm^{-1}$. We employed a linear background correction (a selection of background-corrected spectra are shown in Fig. 4b), and densities of representative chips of AD and LG glasses were measured using a digital Berman balance by comparing the weights of fragments of each glass composition in air and toluene (see Table 1). Sample thickness was measured using a Mitutoyo Elecont Micrometer. Although ε_{3550} has not been calibrated for the melt compositions considered here, a recent compilation of ε_{3550} values for mafic silicate melts by Shishkina et al. (2014) showed that ε_{3550} is relatively insensitive to composition with values ranging from 59.2 ± 4 $l \cdot mol^{-1} \cdot cm^{-1}$ for alkali basalt, basanite, and nephelinite glass compositions (Shishkina et al. 2014) to 68 ± 10 $l \cdot mol^{-1} \cdot cm^{-1}$ for a tholeiitic glass (Shishkina et al. 2010). We adopted an intermediate ε_{3550} of 63 $l \cdot mol^{-1} \cdot cm^{-1}$ for both AD and LG glasses, a value used previously by our lab (Dixon et al. 1995); based on the range of ε_{3550} values reported in the compilation by Shishkina et al. (2014), we expect this value of ε_{3550} to be accurate to better than ~10 %.

3.4. Measuring the total concentration of H-bearing species by SIMS

In addition to measuring the concentration of water (as molecular H_2O and/or OH) by FTIR, we measured the total concentration of H-bearing species in our experimental glasses (dissolved as molecular H_2O, OH, and potentially H_2) using the Cameca 7f-GEO SIMS at Caltech. Prior to analysis, chips of glass from a subset of our experiments (see Table 2) were polished in dental resin. The polished glass chips were removed from the dental resin by soaking in acetone for a few hours and were then ultrasonicated in three cycles each of toluene, acetone, and isopropanol. The chips were baked overnight in a vacuum oven at ~110 °C before being pressed into a 1-inch diameter aluminum mount filled with indium. Three days before the beginning of an analytical session, the mount was coated in a 50-nm layer of gold and was placed under vacuum in the sample storage chamber. Samples were analyzed with a ~4-nA Cs^+ primary beam. The primary beam was rastered across a 15×15 μm^2 area during 120 s of presputtering, and the

area of the raster was reduced to 5×5 μm^2 during analysis. Use of a 100-μm field aperture ensured that only secondary ions from the central ~10 μm of the sputtered crater were collected. Counts of ^{16}OH, ^{18}O, ^{12}C, and ^{30}Si were measured by an electron multiplier. A mass resolving power of ~5000 was used to separate the ^{16}OH peak from ^{17}O. San Carlos olivine containing 0.3 ± 0.1 ppm H_2O (GRR997; Mosenfelder et al. 2011) was analyzed to assess the analytical blank. Five separate analyses of GRR997 produced an average $^{16}OH/^{18}O$ of (7±2)×10^{-4} (error is one standard deviation), which is two-to-three orders of magnitude lower than $^{16}OH/^{18}O$ measured in our experimental glasses (see Table 2). It is also consistent with the independently determined water concentration of 0.3 ppm reported by Mosenfelder et al. (2011) for GRR997; for these reasons, no blank correction has been applied to the $^{16}OH/^{18}O$ measurements reported in Table 2.

4. Results

We conducted 10 experiments on AD (IW–2.3 to IW+4.8; pH_2/pH_2O from 0.003 to 11) and 14 experiments on LG (IW–3.0 to IW+4.8; pH_2/pH_2O from 0.003 to 24). Run conditions are listed in Table 2. The concentrations of total water (i.e., OH + H_2O_{mol}) dissolved in both the LG and AD melts are proportional to $pH_2O^{½}$ (Fig. 5) and range from 69 to 425 ppm (calculated as H_2O by weight). The equations for unweighted least-squares linear regressions of our data are

$$C_{water}^{\mathrm{AD}}\ (ppm) = (727 \pm 13)\sqrt{p\mathrm{H_2O}\ (bar)} \tag{7}$$

$$C_{water}^{\mathrm{LG}}\ (ppm) = (683 \pm 12)\sqrt{p\mathrm{H_2O}\ (bar)}\ , \tag{8}$$

where C_{water}^{AD} is the concentration of total water in AD melt, C_{water}^{LG} is the concentration of total water in LG melt, and errors on the regression coefficients are one standard error. The regressions described by equations (7) and (8) have been forced through the origin; regressions that are not forced through the origin produce best-fit intercepts that are within two standard errors of zero for both the AD and LG compositions.

4.1. Constraints on the concentrations of H-bearing species in our experimental glasses provided by FTIR measurements

Hydroxyl is the only dissolved H-bearing species detected in the quenched glasses. Although we looked for it using FTIR, no molecular water peaks are observed in our spectra at 5200 cm^{-1} or 1630 cm^{-1} (see Fig. 4); likewise, no H_2 was detected by FTIR, and the SIMS analyses coupled with the FTIR measurements are consistent with very limited H_2 in the glasses (see Fig. 4 and Fig. 6; limits on H_2 dissolution based on our SIMS measurements are discussed in section 4.2). The detection limit for the measurement of total water by FTIR using the 3550 cm^{-1} peak is ~10 ppm (based on the noise in our

FTIR spectra). The detection limit for molecular water using the 5200 cm^{-1} combination mode is <100 ppm (e.g., Lesne et al. 2010), and we estimate that the detection limit using the 1630 cm^{-1} fundamental mode is ~25 ppm (assuming a molar absorptivity of 25 l/mol·cm; Dixon et al. 1995). The speciation model described in section 2 and illustrated in Fig. 1 predicts molecular water concentrations of <5 ppm for our experimental glasses with <425 ppm total water (Stolper 1982a; Newman and Lowenstern 2002), so based on these estimated detection limits, the absence of molecular water peaks in our FTIR spectra is to be expected.

The total concentration of dissolved water (which in our glasses is nearly all dissolved as hydroxyl groups) depends only on pH_2O, and is independent of fO_2 and pH_2, i.e., when the pH_2O is the same for experiments on the oxidizing and reducing sides of the pH_2O vs. fO_2 curve (Fig. 3), the dissolved water contents are the same (Fig. 5). Note also that the constants of proportionality in equations (7) and (8) overlap at the two sigma level, suggesting that water solubility is only weakly dependent on melt composition under these conditions. This is further supported by the symmetry of the water concentrations on either side of the pH_2O bell curve in Fig. 5d, despite the extensive Fe-loss suffered by melt in the most reducing LG experiments (due to precipitation of Fe metal; Fig. 2) and the presence of significant concentrations of Fe_2O_3 in the most oxidized LG experiments (up to ~5 wt%; estimated using the calibration of Kress and Carmichael 1991).

4.2. Constraints on the concentrations of H-bearing species in our experimental glasses provided by SIMS measurements

SIMS was used to measure counts of $^{16}OH/^{18}O$ in six AD and seven LG experiments, capturing both high and low pH_2/pH_2O conditions. Unlike FTIR, SIMS is thought to be insensitive to hydrogen speciation (e.g., Hirschmann et al. 2012), so SIMS measurements reflect the total concentration of H-bearing species in the experimental glasses. The expectation, based on the results of Hirschmann et al. (2012) and the simple models discussed in sections 2.1 and 2.2, is that the concentration of dissolved H_2 will increase linearly with pH_2. So if H_2 dissolution in the melts is significant under high pH_2/pH_2O conditions, then SIMS measurements, which reflect total dissolved hydrogen (i.e., the sum of hydroxyl groups, molecular water, and H_2 molecules), would exceed the FTIR measurements (which detect water but not H_2 in our samples). Moreover, any such differences would be expected to increase in a predictable manner as conditions become more reducing because pH_2/pH_2O increases significantly as fO_2 goes down (Fig. 2).

Results from the AD experiments (Fig. 6a) demonstrate that counts of $^{16}OH/^{18}O$ measured by SIMS are directly proportional to the concentration of water measured by FTIR and that both oxidized and reduced experiments for this composition (closed vs. open symbols in Fig. 6a) are consistent with a single regression line. The R^2 value for an unweighted least-squares linear regression of the data in Fig.

6a is 0.99, and the linear relationship between water concentration and $^{16}OH/^{18}O$ accounts for 98.8% of the variance in the data. This is consistent with a negligible role for H_2 dissolution in our AD experiments. We also note that an unweighted linear fit to just the three most oxidized experiments in Fig. 6a (those expected to have the least dissolved H_2) plots nearly atop the plotted regression line and yields a slope and intercept within 1 standard error of those calculated for all six points (the two slopes differ by 2.7%). We have estimated the amount of molecular hydrogen that would be detectable in a hypothetical, H_2-bearing AD glass based on our combined SIMS and FTIR data by calculating a 95% prediction interval for the linear regression in Fig. 6a and asking how much molecular hydrogen could be present in such a glass before its $^{16}OH/^{18}O$ (accounting for 2 sigma errors based on the data in Table 2) would be elevated beyond the 95% prediction interval. The minimum required H_2 is ~4 ppm, thus we conclude that ~4 ppm H_2 can be considered an upper bound on the concentration of H_2 dissolved in our AD experiments. This upper bound is consistent with extrapolation to low pressures of the results of Hirschmann et al. (2012), which suggest that <0.4 ppm H_2 would be soluble in the melts in our experiments.

SIMS measurements of our LG experiments reveal a more complex relationship between counts of $^{16}OH/^{18}O$ measured by SIMS and measurements of water concentration by FTIR: Experiments conducted on the reducing side of the pH_2O bell-shaped curve (open symbols in Fig. 6b) have lower counts of $^{16}OH/^{18}O$ at a given FTIR-measured water concentration than those conducted on the oxidizing side of the pH_2O bell curve (closed symbols in Fig. 6b). This is the opposite of what we might expect if the difference between the oxidized and reduced experiments was due to H_2 dissolution, and instead it likely indicates that counts of $^{16}OH/^{18}O$ are being influenced by changes in the matrix composition. The LG bulk composition contains ~22 wt% FeO (Table 1), but over the large fO_2 range of our experiments, the iron in the LG composition changes from being dominantly metallic iron in coexisting metallic blebs in the most reducing experiments (such that the total amount of FeO dissolved in the melt in these experiments is ~5 times lower than in the experiments at ~IW), to dominantly ferrous iron dissolved in the melt at and above ~IW (Fig. 2), with up to 13 mol.% of the iron dissolved as Fe_2O_3 in our most oxidized LG experiment (according to the calibration of Kress and Carmichael 1991). Changes in the oxidation state of iron are known to affect the physical properties of silicate melts (e.g., Lange and Carmichael 1990; Mysen and Richet 2005), so it is perhaps unsurprising that such a dramatic change in a major component of the LG composition could produce a matrix effect in the SIMS analyses (although there is no such change in water solubility). These results on the LG composition suggest that matrix effects could influence SIMS analyses of water in Fe-rich glass compositions equilibrated over a range of oxygen fugacities, even at very low water concentrations.

In Fig. 7, we explore what the relationship between dissolved H and measured $^{16}OH/^{18}O$ would look like if molecular hydrogen were able to dissolve in our experimental melts in significant quantities.

The calculations shown in Fig. 7 use the relationships between pH_2O and water solubility for AD and LG melts that we have determined [equations (7) and (8)], and assume a molecular hydrogen solubility of 10 ppm by weight per bar of pH_2. This assumed solubility of H_2 is much higher than the expected solubility of H_2 under our experimental conditions [extrapolation to 1 atm of the H_2 solubility experiments of Hirschmann et al. (2012) suggests that only ~0.4 ppm by weight H_2 would be soluble in basaltic melt in equilibrium with 1 bar of pure H_2]. Such a high value for H_2 solubility is chosen for illustrative purposes only; H_2 solubilities from 0 to 10 ppm per bar of pH_2 are considered in Fig. 7c and Fig. 7d. Figure 7a demonstrates for AD melts that there is a strong correlation (R^2=0.99) between $^{16}OH/^{18}O$ measured by SIMS and the concentration of H dissolved as water measured by FTIR. The addition of 10 ppm H_2 per bar of pH_2 would decrease the strength of the correlation between $^{16}OH/^{18}O$ and total dissolved H (R^2=0.91; black squares in Fig. 7a). Although illustrated here for a relatively high H_2 solubility, a decrease in the strength of the correlation between $^{16}OH/^{18}O$ and calculated total dissolved H upon the addition of molecular hydrogen to our AD melts in proportion to their imposed pH_2 is observed for any assumed H_2 solubility (Fig. 7c). Given that $^{16}OH/^{18}O$ measured by SIMS is thought to be proportional to total dissolved H, the calculation in Fig. 7a demonstrates that our SIMS data are consistent with an undetectable solubility of H_2 in our experimental AD melts. Similar arguments can be employed for the LG composition, as illustrated in Fig. 7b and Fig. 7d. The potential role of H_2 dissolution in our experimental melts is discussed further in section 5.3.

5. Discussion

5.1. Comparison to previous work on the solubility of water in basaltic melts

Due to the strong influence of dissolved water in silicate melts on the physical properties of magmas (e.g., density, viscosity, diffusivities of other components) and on volcanic eruptive style (Zhang et al. 2007), there is a large body of existing work dedicated to understanding the dissolution of water in natural silicate melt compositions (McMillan 1994; Moore 2008 and references therein). However, there is little water solubility data for natural silicate-melt compositions in the low water concentration range considered in this study (Friedman et al. 1963; Baker and Grove 1985; Liu et al. 2005). In this section, we compare our water solubility data to existing data for mid-ocean ridge basalt (MORB; Dixon et al. 1995) and basaltic andesite melts (Baker and Grove 1985) and to extrapolations to low pressures of the water solubility models by Newman and Lowenstern (2002), Moore et al. (1998), Papale et al. (2006) and Iacono-Marziano et al. (2012).

Figure 8 shows a comparison between our data and the experimental data of Baker and Grove (1985), who measured the solubility of water in basaltic andesite at 1200–1210 °C and a total pressure of 1 atm. Baker and Grove equilibrated basaltic andesite melts with H_2/CO_2 and H_2/H_2O gas mixtures and

measured the water concentrations in the quenched melts using FTIR. The agreement between our LG and AD solubility experiments, which were conducted at 1350 °C and 1 atm total pressure, and the experiments of Baker and Grove (1985) is consistent with previous conclusions that water solubility in mafic silicate melts is strongly dependent on pH_2O but only weakly dependent on temperature and melt composition (e.g., Newman and Lowenstern 2002; Iacono-Marziano et al. 2012; Shishkina et al. 2014).

Our data are also in good agreement with the water solubility data of Dixon et al. (1995), which were obtained on mid-ocean ridge basalt (MORB) at temperatures of ~1200 °C and pressures of 176–980 bar (Fig. 8). Extrapolations of our results to the conditions of the Dixon et al. experiments using equations (7) and (8) provide good matches to the concentrations of hydroxyl measured by Dixon et al. (1995) but project to lower concentrations than the total water content of these experiments (i.e., the sum of dissolved molecular water and hydroxyl). This is as expected: based on equation (4), a quadratic relationship is expected between the amount of water dissolved as hydroxyl and pH_2O, whereas based on equation (1), a linear (and proportional) relationship is expected between the amount of water dissolved as molecules of water and pH_2O. At low total water contents such those in our vapor-saturated melts, essentially all the dissolved water is present as hydroxyl groups, so the total water content has a quadratic relationship with pH_2O. In the experiments of Dixon et al. (1995), however, pH_2O is high enough that molecular water dissolution is significant, and the proportionality between total water concentration and the square root of pH_2O no longer holds. However, even under these conditions, equation (4) still describes the relationship between the amount of water dissolved as hydroxyl groups and pH_2O, so provided that the solubility of water as hydroxyl groups is not strongly dependent on melt composition, this is consistent with the observation in Fig. 8 that the hydroxyl concentrations of the Dixon et al. experiments plot on the extension of the line defined by the results of our experiments which only contain hydroxyls.

Figure 9 shows comparisons between our experimental data and extrapolations to low pressures of four different water solubility models. Water solubility as predicted by the VolatileCalc model of Newman and Lowenstern (2002) is shown as dashed lines in Fig. 9a. The orange curve shows the model prediction of water solubility (assuming saturation with pure water vapor) at 1350 °C for a basaltic melt with 43 wt% SiO_2 (chosen to match the LG composition) and the blue curve shows the model prediction for a basaltic melt with 49 wt% SiO_2 (this is the maximum SiO_2 content allowed by the VolatileCalc basalt model and was chosen to match, as closely as possible, the AD composition which has ~50 wt% SiO_2). The agreement between this model and our data is good, both in terms of the absolute concentrations of water predicted [the model with 49 wt% SiO_2 predicts water concentrations that are a factor of 1.2 higher than concentrations calculated using equation (7) for the AD composition and the model with 43 wt% SiO_2 predicts water concentrations that are within ~1% of concentrations calculated

using equation (8) for the LG composition] and also in terms of the proportional relationship predicted between water concentration and the square root of pH_2O at these low total water contents. Note that the VolatileCalc model predicts a slight decrease in water solubility with decreasing silica content, and this trend is reflected in our results (although the difference in water solubility between our LG and AD compositions is small and compositional differences other than silica between LG and AD melts could also affect water solubility).

In Fig. 9b, we compare our data to the model of Moore et al. (1998). This model incorporates a parameterization of the dependence of water solubility on the mole fractions of Al_2O_3, FeO^T (all Fe computed as FeO), and Na_2O in the silicate melt, and is designed to be applicable to natural silicate liquids at temperatures of 700–1200 °C and pressures of 1–3000 bar. The Moore model predicts very similar water solubilities in LG and AD melts, despite the large difference in the concentration of FeO^T in these compositions, and this is consistent with the results of our experiments. However, our measured water concentrations are a factor of ~1.6 higher than the Moore et al. model curves at any given pH_2O. This could be explained by ε_{3550} values of 40 l/mol·cm rather than the 63 l/mol·cm we used; however, such a low ε_{3550} is not expected (see discussion in section 3.3). More likely it reflects the large extrapolation from their calibration data set (1.46 to 10.1 wt% dissolved H_2O). Additionally, the Moore et al. model predicts a slight upward curvature of the solubility vs. the square root of pH_2O over the pH_2O range we investigated, which is not observed in our results or expected based on the simple analysis of equations (1) to (4).

In Fig. 9c, our data are compared to the model of Papale et al. (2006). This model aims to capture the effects of melt composition on the shape and position of the volatile saturation surface via a non-ideal, multicomponent, thermodynamic treatment of H_2O-CO_2 solubility in silicate melts. However, this model fails to capture the linear relationship between water concentration and the square root of pH_2O at low pressures that is a robust feature of our results and the simple thermodynamic treatment given above. This likely reflects, at least in part, the fact that the Papale et al. model does not incorporate information about the speciation of volatiles in the melt. The Papale et al. model predicts water concentrations in LG that are a factor of ~4 lower than measured values, and concentrations in AD that are a factor of ~20 lower than our measured values.

Figure 9d compares our data and the H_2O-CO_2 solubility model of Iacono-Marziano et al. (2012) for mafic silicate melts, which was calibrated using experiments at pressures ranging from 100 bar to ~6 kbar and temperatures from 1100 °C to 1400 °C. The water solubility parameterization proposed by Iacono-Marziano et al. (2012) combines the thermodynamic model of Stolper (1982a) with a parameterization of the effect of melt structure (approximated by NBO/O). In their model, the equilibrium concentration of water dissolved in a mafic silicate melt is proportional to $pH_2O^{0.52}$, and over the

concentration range considered in Fig. 9d, the model very closely reproduces the observed linear relationship between water concentration and the square root of pH_2O. The absolute water concentrations predicted by the Iacono-Marziano et al. (2012) model are also in good agreement with our data: The model overestimates the water concentrations measured in our LG experiments by a factor of ~1.4, but provides a good match (within ~10%) for the water concentrations measured in our AD experiments.

In summary, the results of our experiments clearly demonstrate the expected proportional relationship between water solubility and the square root of pH_2O in LG and AD melts equilibrated at low water pressures (pH_2O<~0.3 bar). Models for water solubility in silicate melts must incorporate such a functional form if they are to be applicable at low water concentrations. This simple relationship is expected based on incorporation of the speciation results into simple thermodynamic models (Stolper 1982a; Silver and Stolper 1989; Dixon et al. 1995; Newman and Lowenstern 2002) and it has long been known in the glass industry (Tomlinson 1956; Kurkjian and Russell 1958; Moulson and Roberts 1961; McMillan 1994). We recommend that models and empirical parameterizations of water solubility in silicate melts that do not recover this observed square root dependence at low pressures (e.g., Papale et al. 2006) not be used to predict water solubilities in silicate melts at low pressures.

5.2. Calculation of pH_2O in equilibrium with lunar glasses and melt inclusions

The water solubility relationship for lunar basalt, equation (8), can be used to determine the pH_2O of vapor in equilibrium with lunar glasses and melt inclusions (Saal et al. 2008; Hauri et al. 2011; Saal et al. 2013; Wetzel et al. 2015) at 1350 °C. For example, Wetzel et al. (2015) measured concentration gradients of water and carbon across a single lunar pyroclastic glass bead. The lowest concentration of water measured in this glass bead (at a distance of ~20 µm from the surface of the bead) is 14.5 ppm H_2O_{tot}, which [by applying equation (8)] would be in equilibrium with a vapor having a pH_2O of 0.0005 bar. Assuming an oxygen fugacity of IW−1 for lunar magmas (Sato 1976; Wadhwa 2008) and a temperature of 1350 °C, we can use the gas phase reaction $H_2 + 0.5O_2 \leftrightarrow H_2O$ and its free energy of reaction from Deines et al. (1974) to estimate pH_2 ~0.0011 bar for this vapor. We can thus place a lower limit of ~0.0016 bar on the total vapor pressure of the lunar pyroclastic glass carrier gas, which is consistent with the eruption of this melt into the near-vacuum conditions of the lunar surface. By way of comparison to a terrestrial fire-fountain eruption, Gerlach (1986) reported residual volatile contents (i.e., after eruptive "second-stage" degassing) in Kilauea fire-fountain spatter of approximately 1000 ppm H_2O, 150 ppm S, and <10 ppm CO_2. He applied volatile solubility and mass balance constraints to infer that this melt composition would be in equilibrium with the measured composition of Kilauea Volcano "type II" volcanic gases (containing a mole fraction of H_2O of ~0.8) at total pressures <~3 bar (suggesting a value of pH_2O in the equilibrium vapor of ~2.4 bar). Application of equation (8) to the Kilauea fire-

fountain spatter containing 1000 ppm H_2O implies an equilibrium pH_2O of ~2.1 bar, in good agreement with the results of Gerlach (1986).

The same approach can be used to calculate pCO and pCO_2 in vapor coexisting with the surfaces of molten lunar glass beads. For the lunar glass bead discussed above, Wetzel et al. (2015) obtained a carbon concentration of 0.36 ppm at a distance of ~20 µm from its surface. The speciation and solubility of carbon in reduced lunar melts is currently a topic of debate: Early studies of carbon dissolution in silicate melts under conditions as reducing as ~IW detected no CO species in their quenched melts by FTIR and found that dissolved concentrations of CO_2 in their quenched melts were proportional to the imposed fCO_2, from which they concluded that CO species are insoluble in silicate melts, even under reducing conditions (Pawley et al. 1992; Morizet et al. 2010). More recently, Wetzel et al. (2013) argued for a sharp transition from C dissolution as carbonate at fO_2>IW−0.55 to C dissolution as iron pentacarbonyl and methane at fO_2<IW−0.55. In contrast, a study by Armstrong et al. (2015) argued for a more gradual transition from carbonate dissolution at high fO_2's (>~IW−1) to dissolution of CO species (the exact speciation of the dissolved CO is unclear) at low fO_2's (<~IW−1). Yoshioka et al. (2015) also support the hypothesis that C is dissolved as CO species in melts under reducing conditions. In constructing Fig. 10a, which shows the total gas pressure of vapor (and the partial pressures of the species in the vapor) in equilibrium with melt corresponding in composition to the glass near the surface of lunar glass beads, we consider three different carbon dissolution behaviors:

1. We assume that carbon dissolves entirely as carbonate and we assume the relationship CO_2 (ppm)=0.5×pCO_2 (bar) (Dixon et al. 1995). In this case, for an oxygen fugacity of IW−1, a dissolved C content of 0.36 ppm implies pCO_2 of 2.6 bar and pCO of 20 bar [using the solubility data of Dixon et al. (1995) for MORB and the free energy of reaction for the gas phase reaction $CO + 0.5O_2 \leftrightarrow CO_2$ from Deines et al. (1974)], resulting in a minimum total pressure of 23 bar. These results are shown as the upper bar in Fig. 10a. Lower total pressures would result if the oxygen fugacity was higher.
2. We assume the carbon solubility relationship for reduced lunar glasses (fO_2<IW−0.55) of Wetzel et al. (2013), which is an empirical, linear relationship between dissolved C and total vapor pressure [C (ppm) = 0.2438×P (MPa), where P is pressure]. This relationship predicts that a melt containing 0.36 ppm C (assumed by Wetzel et al. (2013) to be dissolved as iron pentacarbonyl and methane) would be in equilibrium with vapor at a total pressure of ~15 bar (middle bar, Fig. 10a).
3. We assume that carbon dissolves as both carbonate [using the relationship CO_2 (ppm)=0.5×pCO_2 (bar); Dixon et al. 1995] and as CO species [applying equation 10 of Armstrong et al. (2015), which is an empirical relationship relating the concentration of C dissolved in the melt as CO species to $fCO^{0.876}$]. In this case, at an oxygen fugacity of IW−1 at 1350 °C, a dissolved C content of 0.36 ppm

implies pCO_2 of 0.3 bar and pCO of 1.9 bar [using the free energy of reaction for the gas phase reaction $CO + 0.5O_2 \leftrightarrow CO_2$ from Deines et al. (1974) to fix the ratio of pCO to pCO_2], resulting in a minimum total pressure of 2.2 bar. The assumptions of this calculation require 90% of the total C to be dissolved as CO species in order to produce the correct ratio of pCO to pCO_2 (at an oxygen fugacity of IW−1) in the coexisting vapor. These results are shown as the lower bar in Fig. 10a.

Total pressures of 2.2–23 bars would be consistent with vapor equilibration at depths of 53–550 m; such pressures would not be consistent with a vapor cloud erupted into near-vacuum conditions at the lunar surface. The relatively high equilibration pressures suggested by the carbon concentrations of the lunar glasses could reflect kinetic inhibition of carbon degassing (e.g., due to the slower expected diffusion of carbon relative to water in the melt; Zhang and Stolper 1991; Wetzel et al. 2015) and/or a failure to maintain gas-melt equilibrium, perhaps due to the rapid ascent rates expected for lunar pyroclastic eruptions (Rutherford and Papale 2009).

We can also use our water solubility relationship [equation (8)] to constrain the entrapment pressure of lunar olivine-hosted melt inclusions (Hauri et al. 2011; Wetzel et al. 2015). For example, a lunar basaltic melt containing ~1200 ppm water [Hauri et al. (2011), after correction for post-entrapment crystallization] would be in equilibrium with vapor having pH_2O ~3 bar. Using the same procedures as above for pyroclastic beads, assuming IW−1, we estimate pH_2 ~8 bar for this vapor and, thereby a lower limit of ~11 bar for the entrapment pressure of lunar melt inclusions. This corresponds to a minimum depth of ~270 m below the lunar surface (note that this calculation is highly sensitive to fO_2; the calculated pH_2 would increase to ~24 bar at IW−2). The same melt, containing an additional 4 ppm C (e.g., Wetzel et al. 2015) in addition to ~1200 ppm H_2O would imply pCO_2 of 4–29 bar and pCO of 29–220 bar (Fig. 10b), using the same assumptions and solubility data as above, yielding total pressures of 43–260 bar (the total lengths of the lower and upper bars in Fig. 10b) and corresponding to depths within the lunar crust of 1.0–6.3 km. The entrapment pressure would be higher still if the melt was not vapor-saturated at the time of entrapment, or if other gaseous species (e.g., S-bearing species) had significant partial pressures.

Wetzel et al. (2015) did a similar calculation and obtained similar results using the carbon solubility model of Wetzel et al. (2013) and the water solubility from the preliminary report of Newcombe et al. (2012) [i.e., an earlier version of equation (8)]. They inferred equilibration pressures for lunar olivine-hosted melt inclusions of 15–165 bar; these correspond to depths within the lunar crust of 0.3–4 km. When a correction is made for the partitioning of CO and H_2O into vapor bubbles in the melt inclusions, they obtained corrected melt inclusion compositions with vapor saturation pressures of 1870–2760 bar, which roughly correspond to depths of 43–61 km [i.e., below the base of the lunar crust at ~35 km; Wieczorek et al. (2013)]. Wetzel et al. (2015) noted that entrapment depths of ~40 km for their lunar

olivine-hosted melt inclusions are consistent with the estimated depth of the intersection of the orange glass liquidus with the selenotherm of Hess and Parmentier (2001) (with a 10-km thick KREEP layer and >200 times chondritic concentrations of heat-producing elements). However, it should be noted that recent characterizations by Raman spectroscopy of CO_2 vapor densities in vapor bubbles contained within terrestrial olivine-hosted melt inclusions (Steele-Macinnis et al. 2011; Hartley et al. 2014; Moore et al. 2015) have shown that some of these so-called "shrinkage bubbles" (Roedder 1984) contain CO_2 densities that are below the detection limit of Raman spectroscopy (i.e., they appear to contain much lower fCO_2 than expected based on the assumption of equilibrium between the melt and vapor). In light of this, the vapor bubble correction performed by Wetzel et al. (2015) may overestimate the C content, and therefore the entrapment pressure, of their melt inclusions containing vapor bubbles.

The calculations presented above and by Wetzel et al. (2015) demonstrate that, regardless of the uncertainties surrounding the speciation of dissolved C in reduced lunar melts, CO is expected to have been the dominant vapor species in equilibrium with pre-eruptive lunar melts (preserved in olivine-hosted melt inclusions) and in equilibrium with the surfaces of partially degassed lunar pyroclastic glasses.

5.3. Implications for the role of H_2 in lunar magmas

As described in connection with Fig. 6a, our SIMS data for the AD composition places an upper limit on the concentrations of H_2 dissolved in our AD glasses of ~4 ppm. This upper bound is consistent with extrapolation to low pressures of the results of Hirschmann et al. (2012), which suggest that <0.4 ppm H_2 would be soluble in the melts in our experiments. Hirschmann et al. (2012) used their H_2 solubility data and the water solubility model of Moore et al. (1998) to calculate the molar ratio $H_2/(H_2+H_2O)$ dissolved in synthetic basaltic and andesitic melts as a function of pressure, fO_2, and total dissolved H-content. They calculated that, at low pressures (1000 bar), low fO_2's (as low as IW−2), and low total H contents (100 ppm H by wt.) relevant to near-surface lunar melts, molar $H_2/(H_2+H_2O)$ in the melt is < 0.10, from which they concluded that "molecular H_2 is not a significant volatile species for dry magmas at near-surface conditions, such as those from the Moon". Our water solubility relationship for Apollo 15 "yellow glass" predicts water concentrations that are a factor of ~1.6 higher at a given pH_2O than the Moore et al. (1998) model (Fig. 9b), thus the incorporation of our solubility relationship into the calculation of the molar $H_2/(H_2+H_2O)$ ratio by Hirschmann et al. (2012) would predict even lower $H_2/(H_2+H_2O)$ in melts at a given pressure, fO_2, and total H content. Nevertheless, even at this level, both our results and those of Hirschmann et al. (2012) leave room for H_2 dissolution and transport to play a role during syn- and post-fragmentation diffusive degassing of lunar volcanic melts (Wetzel et al. 2015). As described by Zhang (2011) and Sharp et al. (2013), the relative roles of H_2 and H_2O_{mol} during H-component diffusion in silicate melts can be assessed using the ratio of $D_{H_2}[H_2]$ to $D_{H_2O_{mol}}[H_2O_{mol}]$, where D_i is the diffusivity of i in the melt and square brackets indicate molar concentrations; a ratio >1

implies that H_2 is the dominant diffusing H-bearing species. Although there are large uncertainties in both D_{H_2} and $D_{H_2O_{mol}}$ in silicate melts (particularly lunar melts for which data are scarce; Newcombe et al. 2012), Zhang (2011) predicted $D_{H_2}[H_2]/D_{H_2O_{mol}}[H_2O_{mol}]$ ratios of ~4–40 at 1600 K and fO_2 conditions from IW to IW−2. Experiments that explore the transport properties of H-bearing species in silicate melts under reducing conditions would further elucidate the relative importance of diffusive H_2 degassing (compared to degassing of H_2O) during the eruption of lunar melts.

5.4. Which volatile species likely dominated in the vapor that drove lunar fire fountaining?

The propellant (i.e., the dominant species in the vapor) of lunar fire fountain eruptions has long been a topic of debate. Several authors have proposed CO as the primary vapor component (e.g., Housley 1978; Fogel and Rutherford 1995; Nicholis and Rutherford 2009; Rutherford and Papale 2009; Wetzel et al. 2015), and others have proposed H_2 (Sharp et al. 2013; McCubbin et al. 2015). Arguments in support of CO as the primary propellant hinge on the H-depleted nature of lunar magmas compared to most terrestrial magmas (Saal et al. 2008; Hauri et al. 2011; Wetzel et al. 2015; Chen et al. 2015) and on the presence of Fe metal blebs in erupted lunar melts, thought to be the result of the reduction of FeO in the melt in response to graphite oxidation to CO during magma ascent (e.g., Nicholis and Rutherford 2009). Indirect evidence for the presence of graphite in lunar magmas was presented by Sato (1979), who demonstrated that Apollo 17 orange glass undergoes self-reduction upon heating, from which he inferred the presence of ~50 ppm graphite in the magma, although thus far primary igneous graphite has not been found in lunar samples (McCubbin et al. 2015 and references therein).

Recent measurements of dissolved C and H_2O in lunar glasses and improved understanding of C and H_2O solubility in lunar melts (e.g., Saal et al. 2008; Hauri et al. 2011; Wetzel et al. 2013; Chen et al. 2015; Wetzel et al. 2015; this work) warrant a fresh analysis of the major gas species accompanying lunar fire fountaining. In Fig. 11a, we show concentrations of C and H_2O in lunar olivine-hosted melt inclusions and pyroclastic glass beads measured by Saal et al. (2008), Hauri et al. (2011), and Wetzel et al. (2015). The olivine-hosted melt inclusions data represent the most direct constraints on the pre-eruptive volatile contents of lunar magmas (Hauri et al. 2011; Wetzel et al. 2015). Lunar olivine-hosted melt inclusions broadly define a trend that spans water concentrations of ~1200 ppm H_2O to ~270 ppm H_2O and carbon concentrations of ~4 ppm to ~0.36 ppm C. The pyroclastic glass beads shown in Fig. 11a contain only 10s of ppm H_2O and <1 ppm C, and they are thought to have diffusively degassed water and carbon-bearing components after fragmentation (Saal et al. 2008; Wetzel et al. 2015). The initial carbon content of lunar magmas is poorly constrained, but the correction of olivine-hosted melt inclusion compositions for the presence of vapor bubbles led Wetzel et al. (2015) to conclude that primary lunar magmas may have contained ~64 ppm C.

Also shown in Fig. 11a are the results of batch degassing calculations of two lunar melt compositions: The red curve follows the batch degassing path of a melt initially containing 4 ppm C (i.e., the maximum dissolved C concentration in the lunar melt inclusions reported by Wetzel et al. 2015) and 1200 ppm H_2O, and the black curve follows the batch degassing path of a melt initially containing 64 ppm C (i.e., the maximum calculated initial C in lunar melt inclusions, after correcting for the presence of a vapor bubble; Wetzel et al. 2015) and 1200 ppm H_2O. The batch degassing curves in Fig. 11a were calculated using the CO_2 solubility data of Dixon et al. (1995) and the water solubility relationship presented in section 4 [equation (8)]. This approach yields a minimum solubility for C in the melt under reducing conditions because C is also likely to be dissolved in the melt in the form of CO species (e.g., Armstrong et al. 2015). H_2 is assumed to be insoluble in the melt at the low pressures considered here (see discussion in section 5.3). We assume an oxygen fugacity corresponding to IW−1 at 1350 °C (this fixes the H_2/H_2O and CO/CO_2 ratios in the vapor phase; Deines et al. 1974), and we assume that the vapor behaves as an ideal mixture of ideal gases, consistent with expectations for the low pressures and high temperatures considered here (Jakobsson and Oskarsson 1994; Duan 2014). The results of these calculations indicate that carbon exsolves from the melt first, followed by water at lower pressures (<~20 bar for the melt containing 4 ppm C and <~50 bar for the melt containing 64 ppm C).

Figure 11b shows the variation of vapor volume fraction with total pressure based on these calculations, and we use it as the basis for predicting when the exsolved vapor produced by batch degassing could cause fragmentation and drive lunar fire fountaining. We apply a simple vapor volume fraction fragmentation criterion of ~65 to ~75 vol. % vapor (e.g., Spera 1992; Gonnermann and Manga 2012), we assume that the vapor behaves as an ideal mixture of ideal gases, and we assume that the melt has a density of 3000 kg/m^3 (e.g., Rutherford and Papale 2009). This analysis suggests that vapor exsolved by batch degassing from magma initially containing 1200 ppm H_2O and 4–64 ppm reaches the volume fraction required for fragmentation at a pressure of ~5 bar (corresponding to a depth of ~120 m beneath the lunar surface).

Figures 11c and 11d show calculations of the partial pressures of H_2O, H_2, CO_2, and CO in vapors produced by batch degassing of a magma initially containing 1200 ppm H_2O and 64 ppm C at an oxygen fugacity corresponding to IW−1 at a temperature of 1350 °C. Volume percentages of each vapor species are shown in Figs. 11e and 11f. At total pressures >~15 bar, the vapor is dominated by high partial pressures and volume fractions of CO (reflecting the low solubility of C-bearing species relative to H_2O in the melt under these conditions and the significantly higher C/H in the vapor than in the coexisting melt). Only at lower pressures does significant water exsolve from the melt into the vapor and does H_2 become the dominant vapor species; the pressure at which significant H_2O and H_2 begin to appear in the vapor will always be on the same order as (but somewhat higher than) the pressure at which a C-free

system becomes vapor saturated. At the fragmentation pressure (estimated to be ~5 bar; Fig. 11b), the vapor produced by batch degassing contains ~59 vol. % H_2 and only ~15 vol. % CO; therefore, the results of our calculations support the hypothesis that H_2, rather than CO, was the primary propellant of the lunar fire fountain eruptions. We tested the sensitivity of this result to variations in the initial C content of the melt, and find that initial melt compositions with >~200 ppm C would be required for vapor compositions to be dominated by CO rather than H_2 at 65–75 % vesicularity. The vapor composition at the fragmentation pressure becomes even more H_2-rich if we assume that C is dissolved in the melt as CO species (i.e., by applying equation 10 of Armstrong et al. 2015). This is because the assumption that C is able to dissolve in the melt as CO increases the net solubility of C in the melt under reducing conditions where the coexisting vapor is much richer in CO than CO_2 (e.g., at IW−1 and 1350 °C, the ratio of pCO to $p\mathrm{CO}_2$ in the vapor is ~7.6 according to the free energy of reaction for the gas phase reaction $\mathrm{CO} + 0.5\mathrm{O}_2 \leftrightarrow \mathrm{CO}_2$ of Deines et al. 1974). We note that the simple treatment described here does not account for the presence of S-bearing species, which may well have contributed to the vapor phase responsible for driving lunar fire fountaining (e.g., Elkins-Tanton et al. 2003) and may also have acted as a sink for H_2 via the formation of H_2S in the vapor. We also note that, although the calculations described above may remove the requirement that large quantities of C be present in lunar magmas to drive fire fountain eruptions, early degassing of CO from lunar magmas may still be required to provide the buoyancy needed for the magmas to rise through the lunar crust (Nicholis and Rutherford 2009).

We note that there is an apparent inconsistency between the CO-rich vapor composition in equilibrium with the lunar glass bead in Fig. 10a and the H_2-rich vapor composition produced by batch degassing of lunar melts to low pressures (Fig. 11d). As discussed at the end of section 5.2, the elevated carbon concentrations of the lunar glasses compared to the low pressure portion of our batch degassing model (<5 bar) could reflect kinetic inhibition of carbon degassing (e.g., due to the slower expected diffusion of carbon relative to water in the melt; Zhang and Stolper 1991; Wetzel et al. 2015) and/or a failure to maintain gas-melt equilibrium, perhaps due to the rapid ascent rates expected for lunar pyroclastic eruptions (Rutherford and Papale 2009). There is also a large discrepancy between the melt inclusion data and our batch degassing model at higher pressures on Fig. 11a. Most of the melt inclusion data would be better described by a batch degassing model with an initial melt composition containing ~750 ppm H_2O. We have calculated batch degassing of a melt initially containing 750 ppm H_2O and 64 ppm C (not shown on Fig. 11), and our conclusion that the vapor composition at the fragmentation pressure is dominated by H_2 also holds for this initial melt composition; however, we chose an initial H_2O concentration corresponding to the maximum measured H_2O in the lunar melt inclusions (1200 ppm) for Fig. 11, because some or all of the melt inclusions in Fig. 11a could have been affected by post-entrapment diffusive loss of H^+ (e.g., Bucholz et al. 2013).

We emphasize that the presence of high volume fractions of H_2 in the integrated vapor exsolved from lunar melts at low pressures (no more than a few 10s of bar) does not imply high quantities of dissolved H_2 in the pre-eruptive melts (which would be inconsistent with the experimental results presented in sections 4.1 and 4.2). Instead, if at each stage of the degassing process the melt in contact with the vapor is in equilibrium, the H is dissolved in lunar melts primarily as hydroxyl, but upon degassing of this hydroxyl as molecular water, equilibration of the vapor to the prevailing fO_2 of the system (thought to be ~IW−1) results in reduction of the H_2O exsolving from the melt to an H_2-rich gas (perhaps via back-reaction with the melt, or by exchanging oxygen with other vapor species such as C-bearing or S-bearing species).

6. Conclusions

1. We report the solubility of water in synthetic lunar basaltic melt and an iron-free basaltic analog composition at 1 atm and 1350 °C. Our experiments span ~8 orders of magnitude in fO_2 (IW−3.0 to IW+4.8) and ~4 orders of magnitude in pH_2/pH_2O (from 0.003 to 24), and our quenched experimental melts contain 69–425 ppm total water.
2. The solubility of water in lunar basaltic melt in equilibrium with a C-O-H vapor at 1350 °C and 1 atm is proportional to the square root of pH_2O in the vapor phase, and is independent of fO_2 (and therefore to pH_2/pH_2O).
3. Caution must be used in extrapolating water solubility models constrained by higher-pressure water-solubility data to the low pH_2O conditions considered in this study. Models that do not incorporate water speciation at low total water concentrations are typically unable to reproduce the proportional relationship between water solubility and the square root of pH_2O that is a robust feature of our results.
4. Hydroxyl is the only H-bearing species detected in our experiments by FTIR. Comparison of the FTIR results with SIMS measurements of our iron-free experimental glasses constrain the concentration of H dissolved as H_2 to be <~4 ppm, consistent with extrapolation to 1 atm of measurements of H_2 solubility in basalt by Hirschmann et al. (2012) that suggest a solubility of H_2 of ~0.4 ppm (weight). Our data may suggest evidence for matrix effects in SIMS measurements of water in iron-rich glasses equilibrated over a range of fO_2 conditions.
5. Our results constrain the pH_2O of vapor in equilibrium with lunar glasses and melt inclusions. We find that, at 1350 °C and IW−1, the most water-rich melt inclusion of Hauri et al. (2011) would be in equilibrium with a vapor with pH_2O ~3 bar and pH_2 ~8 bar. Consideration of the dissolved concentration of carbon in lunar melt inclusions characterized by Wetzel et al. (2015) allows an estimate of lower bounds for the entrapment pressures of these melt inclusions of 43–260 bar,

corresponding to depths within the lunar crust of 1.0–6.3 km. We also constrain the partial pressures of water and molecular hydrogen in the carrier gas of the lunar pyroclastic glass beads to be 0.0005 bar and 0.0011 bar respectively; such low pressures of H-bearing species are consistent with eruption into the near-vacuum conditions at the lunar surface. By way of comparison, similar calculations for terrestrial fire-fountain deposits (Kilauea Iki fire-fountain spatter containing ~1000 ppm water) predict partial pressures of water in their carrier gas of ~2.1–2.4 bar.

6. Batch degassing calculations of lunar melts containing initial volatile contents of 1200 ppm H_2O and 4–64 ppm C indicate that exsolved vapor compositions are dominated by H_2 at total pressures <~15 bar. Assuming that fragmentation occurs at vapor volume fractions of ~65–75 vol. %, these calculations indicate a fragmentation pressure of ~5 bar, corresponding to a depth within the lunar crust of ~120 m. These results indicate that H_2 was the primary propellant of the lunar fire fountain eruptions.

7. Acknowledgements

We would like to thank Paul Asimow for donating anorthite-diopside glass for use in this study. We would also like to thank Chi Ma for his advice and assistance with operation of the electron microprobe. We are grateful to Paul Asimow, George Rossman, and Dave Stevenson for many enlightening discussions. We are also grateful for thoughtful reviews by Malcolm Rutherford, Stephen Elardo, and an anonymous reviewer. Newcombe gratefully acknowledges financial support from a NASA Earth and Space Sciences Fellowship (PLANET14R-0040).

8. References

Albarède F., Albalat E. and Lee C.-T.A. (2015) An intrinsic volatility scale relevant to the Earth and Moon and the status of water in the Moon. *Meteoritics & Planetary Science* **50**, 568-577.

Ardia P., Hirschmann M.M., Withers A.C. and Stanley B.D. (2013) Solubility of CH_4 in a synthetic basaltic melt, with applications to atmosphere–magma ocean–core partitioning of volatiles and to the evolution of the Martian atmosphere. *Geochimica et Cosmochimica Acta* **114**, 52-71.

Armstrong J.T. (1988) Quantitative analysis of silicate and oxide minerals: Comparison of Monte Carlo, ZAF and $\phi(\rho z)$ procedures. San Francisco Press, San Francisco.

Armstrong L.S., Hirschmann M.M., Stanley B.D., Falksen E.G. and Jacobsen S.D. (2015) Speciation and solubility of reduced C–O–H–N volatiles in mafic melt: Implications for volcanism, atmospheric evolution, and deep volatile cycles in the terrestrial planets. *Geochimica et Cosmochimica Acta* **171**, 283-302.

Asimow P.D. and Ahrens T.J. (2010) Shock compression of liquid silicates to 125 GPa: The anorthite-diopside join. *Journal of Geophysical Research: Solid Earth* **115**.

Baker M.B. and Grove T.L. (1985) Kinetic controls on pyroxene nucleation and metastable liquid lines of descent in a basaltic andesite. *American Mineralogist* **70**, 279-287.

Barnes J.J., Tartèse R., Anand M., McCubbin F.M., Franchi I.A., Starkey N.A. and Russell S.S. (2014) The origin of water in the primitive Moon as revealed by the lunar highlands samples. *Earth and Planetary Science Letters* **390**, 244-252.

Beckett J.R. and Mendybaev R.A. (1997) The measurement of oxygen fugacities in flowing gas mixtures at temperatures below 1200°C. *Geochimica et Cosmochimica Acta* **61**, 4331-4336.

Behrens H., Misiti V., Freda C. and Vetere F. (2009) Solubility of H_2O and CO_2 in ultrapotassic melts at 1200 and 1250 °C and pressure from 50 to 500 MPa. *American Mineralogist* **94**, 105.

Behrens H. and Nowak M. (1997) The mechanisms of water diffusion in polymerized silicate melts. *Contributions to Mineralogy and Petrology* **126**, 377-385.

Bell P., Mao H. and Weeks R. (1976) Optical spectra and electron paramagnetic resonance of lunar and synthetic glasses-A study of the effects of controlled atmosphere, composition, and temperature, *Proceedings of the 7th Lunar and Planetary Science Conference*, 2543-2559.

Benne D. and Behrens H. (2003) Water solubility in haplobasaltic melts. *European Journal of Mineralogy* **15**, 803-814.

Berndt J., Liebske C., Holtz F., Freise M., Nowak M., Ziegenbein D., Hurkuck W. and Koepke J. (2002) A combined rapid-quench and H_2-membrane setup for internally heated pressure vessels: Description and application for water solubility in basaltic melts. *American Mineralogist* **87**, 1717.

Borisov A. and Jones J.H. (1999) An evaluation of Re, as an alternative to Pt, for the 1 bar loop technique: An experimental study at 1400 . *American Mineralogist* **84**, 1528-1534.

Boyce J.W., Liu Y., Rossman G.R., Guan Y., Eiler J.M., Stolper E.M. and Taylor L.A. (2010) Lunar apatite with terrestrial volatile abundances. *Nature* **466**, 466-469.

Bucholz C.E., Gaetani G.A., Behn M.D., and Shimizu N. (2013) Post-entrapment modification of volatiles and oxygen fugacity in olivine-hosted melt inclusions. *Earth and Planetary Science Letters* **374**, 145-155.

Burgisser A., Alletti M. and Scaillet B. (2015) Simulating the behavior of volatiles belonging to the C–O–H–S system in silicate melts under magmatic conditions with the software D-Compress. *Computers & Geosciences* **79**, 1-14.

Canup R.M. and Asphaug E. (2001) Origin of the Moon in a giant impact near the end of the Earth's formation. *Nature* **412**, 708-712.

Canup R.M., Visscher C., Salmon J. and Fegley Jr B. (2015) Lunar volatile depletion due to incomplete accretion within an impact-generated disk. *Nature Geoscience* **8**, 918-921.

Chen Y., Zhang Y., Liu Y., Guan Y., Eiler J. and Stolper E.M. (2015) Water, fluorine, and sulfur concentrations in the lunar mantle. *Earth and Planetary Science Letters* **427**, 37-46.

Chertkova N. and Yamashita S. (2015) In situ spectroscopic study of water speciation in the depolymerized $Na_2Si_2O_5$ melt. *Chemical Geology* **409**, 149-156.

Deines P., Nafziger R.H., Ulmer G.C. and Woermann E. (1974) Temperature - oxygen fugacity tables for selected gas mixtures in the system C-H-O at one atmosphere total pressure. *Bulletin of the Earth and Mineral Sciences Experiment Station*.

Delano J. (1980) Apollo 15 yellow glasses: Chemistry and possible origins, Lunar and Planetary Science Conference, pp. 213-215.

Delano J.W. (1986) Pristine lunar glasses: Criteria, data, and implications. *Journal of Geophysical Research* **91**, D201-D213.

Dingwell D.B. and Webb S.L. (1990) Relaxation in silicate melts. *European Journal of Mineralogy* **2**, 427-449.

Dixon J.E., Stolper E.M. and Holloway J.R. (1995) An experimental study of water and carbon dioxide solubilities in mid-ocean ridge basaltic liquids. Part I: Calibration and solubility models. *Journal of Petrology* **36**, 1607-1631.

Duan X. (2014) A general model for predicting the solubility behavior of H_2O–CO_2 fluids in silicate melts over a wide range of pressure, temperature and compositions. *Geochimica et Cosmochimica Acta* **125**, 582-609.

Elkins-Tanton, L.T., Chatterjee, N., and Grove, T.L. (2003) Magmatic processes that produced lunar fire fountains, *Geophysical Research Letters* **30**, 1513, doi:10.1029/2003GL017082, 10.

Elkins-Tanton L.T. and Grove T.L. (2011) Water (hydrogen) in the lunar mantle: Results from petrology and magma ocean modeling. *Earth and Planetary Science Letters* **307**, 173-179.

Fogel R.A. and Rutherford M.J. (1995) Magmatic volatiles in primitive lunar glasses: I. FTIR and EPMA analyses of Apollo 15 green and yellow glasses and revision of the volatile-assisted fire-fountain theory. *Geochimica et Cosmochimica Acta* **59**, 201-215.

Friedman I., Hardcastle K.G. and Gleason J.D. (1974) Isotopic composition of carbon and hydrogen in some Apollo 14 and 15 lunar samples. *Journal of Research of the U.S. Geological Survey* **2**, 7-12.

Friedman I., Long W. and Smith R.L. (1963) Viscosity and water content of rhyolite glass. *Journal of Geophysical Research* **68**, 6523-6535.

Füri E., Deloule E., Gurenko A. and Marty B. (2014) New evidence for chondritic lunar water from combined D/H and noble gas analyses of single Apollo 17 volcanic glasses. *Icarus* **229**, 109-120.

Gerlach T.M. (1986) Exsolution of H_2O, CO_2, and S during eruptive episodes at Kilauea Volcano, Hawaii. *Journal of Geophysical Research: Solid Earth (1978–2012)* **91**, 12177-12185.

Gonnermann H. M. and Manga M. (2013) Dynamics of magma ascent in the volcanic conduit. *Modeling volcanic processes: The physics and mathematics of volcanism*, 55.

Goranson R.W. (1931) Solubility of water in granite magmas. *Eos, Transactions American Geophysical Union* **12**, 183-183.

Greenwood J.P., Itoh S., Sakamoto N., Warren P., Taylor L. and Yurimoto H. (2011) Hydrogen isotope ratios in lunar rocks indicate delivery of cometary water to the Moon. *Nature Geoscience* **4**, 79-82.

Hamilton D.L., Burnham C.W. and Osborn E.F. (1964) The solubility of water and effects of oxygen fugacity and water content on crystallization in mafic magmas. *Journal of Petrology* **5**, 21-39.

Hartley M.E., Maclennan J., Edmonds M. and Thordarson T. (2014) Reconstructing the deep CO_2 degassing behaviour of large basaltic fissure eruptions. *Earth and Planetary Science Letters* **393**, 120-131.

Hauri E.H., Saal A.E., Rutherford M.J. and Van Orman J.A. (2015) Water in the Moon's interior: Truth and consequences. *Earth and Planetary Science Letters* **409**, 252-264.

Hauri E.H., Weinreich T., Saal A.E., Rutherford M.C. and Van Orman J.A. (2011) High pre-eruptive water contents preserved in lunar melt inclusions. *Science* **333**, 213-215.

Hess P., Rutherford M., Guillemette R., Ryerson F. and Tuchfeld H. (1975) Residual products of fractional crystallization of lunar magmas-an experimental study, *Proceedings of the 6th Lunar and Planetary Science Conference*, 895-909.

Hess P.C. and Parmentier E.M. (2001) Thermal evolution of a thicker KREEP liquid layer. *Journal of Geophysical Research: Planets* **106**, 28023-28032.

Hirschmann M.M., Withers A.C., Ardia P. and Foley N.T. (2012) Solubility of molecular hydrogen in silicate melts and consequences for volatile evolution of terrestrial planets. *Earth and Planetary Science Letters* **345–348**, 38-48.

Housley R.M. (1978) Modeling lunar volcanic eruptions. *Proceedings of the 9th Lunar and Planetary Science Conference* 1473-1484.

Huebner J.S. (1971) Buffering techniques for hydrostatic systems at elevated pressures, in: Ulmer, G. (Ed.), Research Techniques for High Pressure and High Temperature. Springer Berlin Heidelberg, pp. 123-177.

Hui H., Peslier A.H., Zhang Y. and Neal C.R. (2013) Water in lunar anorthosites and evidence for a wet early Moon. *Nature Geosci* **6**, 177-180.

Iacono-Marziano G., Morizet Y., Le Trong E. and Gaillard F. (2012) New experimental data and semi-empirical parameterization of H_2O–CO_2 solubility in mafic melts. *Geochimica et Cosmochimica Acta* **97**, 1-23.

Jakobsson S. and Oskarsson N. (1994) The system C-O in equilibrium with graphite at high pressure and temperature: An experimental study. *Geochimica et Cosmochimica Acta* **58**, 9-17.

Kohn S.C. (2000) The dissolution mechanisms of water in silicate melts; a synthesis of recent data. *Mineralogical Magazine* **64**, 389-408.

Kress V. and Carmichael I.E. (1991) The compressibility of silicate liquids containing Fe_2O_3 and the effect of composition, temperature, oxygen fugacity and pressure on their redox states. *Contributions to Mineralogy and Petrology* **108**, 82-92.

Kurkjian C. and Russell L. (1958) Solubility of water in molten alkali silicates. *J. Soc. Glass Technol* **42**, 130-144.

Lange R.L. and Carmichael I.S.E. (1990) Thermodynamic properties of silicate liquids with emphasis on density, thermal expansion and compressibility. *Reviews in Mineralogy and Geochemistry* **24**, 25-64.

Le Losq C., Mysen B.O. and Cody G.D. (2015) Water and magmas: insights about the water solution mechanisms in alkali silicate melts from infrared, Raman, and ^{29}Si solid-state NMR spectroscopies. *Progress in Earth and Planetary Science* **2**, 1-16.

Lesne P., Scaillet B., Pichavant M., Iacono-Marziano G. and Beny J.-M. (2010) The H_2O solubility of alkali basaltic melts: an experimental study. *Contributions to Mineralogy and Petrology* **162**, 133-151.

Liu Y., Zhang Y. and Behrens H. (2005) Solubility of H_2O in rhyolitic melts at low pressures and a new empirical model for mixed H_2O–CO_2 solubility in rhyolitic melts. *Journal of Volcanology and Geothermal Research* **143**, 219-235.

McCubbin F.M., Steele A., Hauri E.H., Nekvasil H., Yamashita S. and Hemley R.J. (2010) Nominally hydrous magmatism on the Moon. *Proceedings of the National Academy of Sciences* **107**, 11223-11228.

McCubbin F.M., Vander Kaaden K.E., Tartèse R., Klima R.L., Liu Y., Mortimer J., Barnes J.J., Shearer C.K., Treiman A.H., Lawrence D.J., Elardo S.M., Hurley D.M., Boyce J.W. and Anand M. (2015) Magmatic volatiles (H, C, N, F, S, Cl) in the lunar mantle, crust, and regolith: Abundances, distributions, processes, and reservoirs. *American Mineralogist* **100**, 1668-1707.

McMillan P.F. (1994) Water solubility and speciation models. *Reviews in Mineralogy and Geochemistry* **30**, 132-156.

Moore G. (2008) Interpreting H_2O and CO_2 contents in melt inclusions: constraints from solubility experiments and modeling. *Reviews in Mineralogy and Geochemistry* **69**, 333-362.

Moore G., Vennemann T. and Carmichael I. (1998) An empirical model for the solubility of H_2O in magmas to 3 kilobars. *American Mineralogist* **83**, 36-42.

Moore L.R., Gazel E., Tuohy R., Lloyd A.S., Esposito R., Steele-MacInnis M., Hauri E.H., Wallace P.J., Plank T. and Bodnar R.J. (2015) Bubbles matter: An assessment of the contribution of vapor bubbles to melt inclusion volatile budgets. *American Mineralogist* **100**, 806-823.

Morizet Y., Paris M., Gaillard F. and Scaillet B. (2010) C–O–H fluid solubility in haplobasalt under reducing conditions: An experimental study. *Chemical Geology* **279**, 1-16.

Mosenfelder J.L., Voyer Marion L., Rossman George R., Guan Y., Bell David R., Asimow Paul D. and Eiler John M. (2011) Analysis of hydrogen in olivine by SIMS: Evaluation of standards and protocol. *American Mineralogist* **96**, 1725.

Moulson A. and Roberts J. (1961) Water in silica glass. *Transactions of the Faraday Society* **57**, 1208-1216.

Mysen B. and Richet P. (2005) Silicate glasses and melts: Properties and structure. Elsevier.

Mysen B.O., Fogel M.L., Morrill P.L. and Cody G.D. (2009) Solution behavior of reduced COH volatiles in silicate melts at high pressure and temperature. *Geochimica et Cosmochimica Acta* **73**, 1696-1710.

Mysen B.O., Kumamoto K., Cody G.D. and Fogel M.L. (2011) Solubility and solution mechanisms of C–O–H volatiles in silicate melt with variable redox conditions and melt composition at upper mantle temperatures and pressures. *Geochimica et Cosmochimica Acta* **75**, 6183-6199.

Mysen B.O. and Yamashita S. (2010) Speciation of reduced C–O–H volatiles in coexisting fluids and silicate melts determined in-situ to □1.4 GPa and 800 °C. *Geochimica et Cosmochimica Acta* **74**, 4577-4588.

Nakajima M. and Stevenson D. (2014) Hydrodynamic escape does not prevent the "wet" Moon formation, *Proceedings of the 45th Lunar and Planetary Science Conference*, 2770.

Newcombe M., Brett A., Beckett J., Baker M., Newman S. and Stolper E. (2012) Solubility and diffusivity of H-bearing species in lunar basaltic melts, *Proceedings of the 43rd Lunar and Planetary Science Conference*, 2777.

Newman S. and Lowenstern J.B. (2002) VolatileCalc: a silicate melt–H_2O–CO_2 solution model written in Visual Basic for excel. *Computers & Geosciences* **28**, 597-604.

Newman S., Stolper E.M. and Epstein S. (1986) Measurement of water in rhyolitic glasses--calibration of an infrared spectroscopic technique. *American Mineralogist* **71**, 1527-1541.

Newsom H.E. and Taylor S.R. (1989) Geochemical implications of the formation of the Moon by a single giant impact. *Nature* **338**, 29-34.

Nicholis M.G. and Rutherford M.J. (2009) Graphite oxidation in the Apollo 17 orange glass magma: Implications for the generation of a lunar volcanic gas phase. *Geochimica et Cosmochimica Acta* **73**, 5905-5917.

Nowak M. and Behrens H. (2001) Water in rhyolitic magmas: Getting a grip on a slippery problem. *Earth and Planetary Science Letters* **184**, 515-522.

O'Neill H.C. and Pownceby M. (1993) Thermodynamic data from redox reactions at high temperatures. I. An experimental and theoretical assessment of the electrochemical method using stabilized zirconia electrolytes, with revised values for the Fe-"FeO", Co-CoO, Ni-NiO and Cu-Cu_2O oxygen buffers, and new data for the W-WO_2 buffer. *Contributions to Mineralogy and Petrology* **114**, 296-314.

O'Neill H.S. (1987) Quartz-fayalite-iron and quartz-fayalite-magnetite equilibria and the free energy of formation of fayalite (Fe_2SiO_4) and magnetite (Fe_3O_4). *American Mineralogist* **72**, 67-75.

Orlova G.P. (1964) Solubility of water in albite melts under pressure. *International Geology Review* **6**, 254-258.

Pahlevan K. and Stevenson D.J. (2007) Equilibration in the aftermath of the lunar-forming giant impact. *Earth and Planetary Science Letters* **262**, 438-449.

Papale P., Moretti R. and Barbato D. (2006) The compositional dependence of the saturation surface of H_2O + CO_2 fluids in silicate melts. *Chemical Geology* **229**, 78-95.

Pawley A.R., Holloway J.R. and McMillan P.F. (1992) The effect of oxygen fugacity on the solubility of carbon–oxygen fluids in basaltic melt. *Earth and Planetary Science Letters* **110**, 213-225.

Persikov E.S., Newman S., Bukhtiyarov P.G., Nekrasov A.N. and Stolper E.M. (2010) Experimental study of water diffusion in haplobasaltic and haploandesitic melts. *Chemical Geology* **276**, 241-256.

Pineau F., Shilobreeva S., Kadik A. and Javoy M. (1998) Water solubility and D/H fractionation in the system basaltic andesite–H_2O at 1250°C and between 0.5 and 3 kbars. *Chemical Geology* **147**, 173-184.

Pownceby M.I. and O'Neill H.S.C. (1994) Thermodynamic data from redox reactions at high temperatures. IV. Calibration of the Re-ReO_2 oxygen buffer from EMF and NiO+ Ni-Pd redox sensor measurements. *Contributions to Mineralogy and Petrology* **118**, 130-137.

Roedder E. (1984) Fluid Inclusions. Mineralogical Society of America.

Rutherford M.J. and Papale P. (2009) Origin of basalt fire-fountain eruptions on Earth versus the Moon. *Geology* **37**, 219-222.

Saal A.E., Hauri E.H., Cascio M.L., Van Orman J.A., Rutherford M.C. and Cooper R.F. (2008) Volatile content of lunar volcanic glasses and the presence of water in the Moon's interior. *Nature* **454**, 192-195.

Saal A.E., Hauri E.H., Van Orman J.A. and Rutherford M.J. (2013) Hydrogen isotopes in lunar volcanic glasses and melt inclusions reveal a carbonaceous chondrite heritage. *Science* **340**, 1317-1320.

Sato M. (1976) Oxygen fugacity and other thermochemical parameters of Apollo 17 high-Ti basalts and their implications on the reduction mechanism, *Proceedings of the 7th Lunar and Planetary Science Conference*, 1323-1344.

Sato M. (1979) The driving mechanism of lunar pyroclastic eruptions inferred from the oxygen fugacity behavior of Apollo 17 orange glass. *Proceedings of the 10th Lunar and Planetary Science Conference*, 311-325.

Sharp Z.D., McCubbin F.M. and Shearer C.K. (2013) A hydrogen-based oxidation mechanism relevant to planetary formation. *Earth and Planetary Science Letters* **380**, 88-97.

Sharp Z.D., Shearer C.K., McKeegan K.D., Barnes J.D. and Wang Y.Q. (2010) The chlorine isotope composition of the Moon and implications for an anhydrous mantle. *Science* **329**, 1050-1053.

Shishkina T.A., Botcharnikov R.E., Holtz F., Almeev R.R., Jazwa A.M. and Jakubiak A.A. (2014) Compositional and pressure effects on the solubility of H_2O and CO_2 in mafic melts. *Chemical Geology* **388**, 112-129.

Shishkina T.A., Botcharnikov R.E., Holtz F., Almeev R.R. and Portnyagin M.V. (2010) Solubility of H_2O- and CO_2-bearing fluids in tholeiitic basalts at pressures up to 500 MPa. *Chemical Geology* **277**, 115-125.

Sieverts A. (1929) Absorption of gases by metals. *Z. Metallkund* **21**, 37.

Silver L., Ihinger P. and Stolper E. (1990) The influence of bulk composition on the speciation of water in silicate glasses. *Contributions to Mineralogy and Petrology* **104**, 142-162.

Silver L. and Stolper E. (1989) Water in albitic glasses. *Journal of Petrology* **30**, 667-709.

Sowerby J.R. and Keppler H. (1999) Water speciation in rhyolitic melt determined by in-situ infrared spectroscopy. *American Mineralogist* **84**, 1843-1849.

Spera F.J. (1992) Lunar magma transport phenomena. *Geochimica et Cosmochimica Acta* **56**, 2253-2265.

Steele-Macinnis M., Esposito R. and Bodnar R.J. (2011) Thermodynamic model for the effect of post-entrapment crystallization on the H_2O–CO_2 systematics of vapor-saturated, silicate melt inclusions. *Journal of Petrology* **52**, 2461-2482.

Stolper E. (1982a) The speciation of water in silicate melts. *Geochimica et Cosmochimica Acta* **46**, 2609-2620.

Stolper E. (1982b) Water in silicate glasses: An infrared spectroscopic study. *Contributions to Mineralogy and Petrology* **81**, 1-17.

Stolper E. (1989) Temperature dependence of the speciation of water in rhyolitic melts and glasses. *American Mineralogist* **74**, 1247-1257.

Tartèse R., Anand M., McCubbin F.M., Elardo S.M., Shearer C.K. and Franchi I.A. (2014) Apatites in lunar KREEP basalts: The missing link to understanding the H isotope systematics of the Moon. *Geology* **42**, 363-366.

Taylor W. and Green D. (1987) The petrogenetic role of methane: effect on liquidus phase relations and the solubility mechanism of reduced C–H volatiles, Magmatic processes: physicochemical principles. Geochemical Society University PArk, PA, pp. 121-138.

Tomlinson J. (1956) A note on the solubility of water in a molten sodium silicate. *J. Soc. Glass Technol* **40**, 25T-31T.

Wadhwa M. (2008) Redox conditions on small bodies, the Moon and Mars. *Reviews in Mineralogy and Geochemistry* **68**, 493-510.

Wetzel D.T., Hauri E.H., Saal A.E. and Rutherford M.J. (2015) Carbon content and degassing history of the lunar volcanic glasses. *Nature Geoscience* **8**, 755-758.

Wetzel D.T., Rutherford M.J., Jacobsen S.D., Hauri E.H. and Saal A.E. (2013) Degassing of reduced carbon from planetary basalts. *Proceedings of the National Academy of Sciences* **110**, 8010-8013.

Wieczorek M.A., Neumann G.A., Nimmo F., Kiefer W.S., Taylor G.J., Melosh H.J., Phillips R.J., Solomon S.C., Andrews-Hanna J.C., Asmar S.W., Konopliv A.S., Lemoine F.G., Smith D.E., Watkins M.M., Williams J.G. and Zuber M.T. (2013) The Crust of the Moon as Seen by GRAIL. *Science* **339**, 671-675.

Withers A.C., Zhang Y. and Behrens H. (1999) Reconciliation of experimental results on H_2O speciation in rhyolitic glass using in-situ and quenching techniques. *Earth and Planetary Science Letters* **173**, 343-349.

Yoshioka, T., McCammon, C., Shcheka, S., & Keppler, H. (2015) The speciation of carbon monoxide in silicate melts and glasses. *American Mineralogist*, **100**, 1641-1644.

Zhang C. and Duan Z. (2009) A model for C–O–H fluid in the Earth's mantle. *Geochimica et Cosmochimica Acta* **73**, 2089-2102.

Zhang Y. (1999) H_2O in rhyolitic glasses and melts: Measurement, speciation, solubility, and diffusion. *Reviews of Geophysics* **37**, 493-516.

Zhang Y. (2011) "Water" in lunar basalts: The role of molecular hydrogen (H_2), especially in the diffusion of the H component, *Proceedings of the 42nd Lunar and Planetary Science Conference*.

Zhang Y. and Ni H. (2010) Diffusion of H, C, and O components in silicate melts. *Reviews in Mineralogy and Geochemistry* **72**, 171-225.

Zhang Y. and Stolper E.M. (1991) Water diffusion in a basaltic melt. *Nature* **351**, 306-309.

Zhang Y., Stolper E.M. and Wasserburg G.J. (1991) Diffusion of a multi-species component and its role in oxygen and water transport in silicates. *Earth and Planetary Science Letters* **103**, 228-240.

Zhang Y., Xu Z., Zhu M. and Wang H. (2007) Silicate melt properties and volcanic eruptions. *Reviews of Geophysics* **45**

	$An_{36}Di_{64}$ target	*AD Batch 1*		*AD Batch 3*		*Apollo 15 'yellow glass'*	*LG composition*	
Oxide (wt%)	nominal concentration	mean	1 σ	mean	1 σ	nominal concentration	mean	1 σ
SiO_2	50.33	49.35	0.65	49.94	0.32	43.05	43.62	0.19
TiO_2	0.00	b.d.		0.019	0.022	3.49	3.46	0.04
Al_2O_3	15.37	18.51	0.74	16.58	0.28	8.33	8.96	0.05
FeO*	0.00	0.034	0.028	0.020	0.021	22.18	21.78	0.35
MgO	10.80	9.31	0.20	10.46	0.07	13.55	13.10	0.07
CaO	23.49	23.60	0.10	23.90	0.09	8.53	8.74	0.03
Na_2O	0.00	0.061	0.012	0.084	0.021	0.00	0.005	0.007
K_2O	0.00	b.d.		0.010	0.007	0.00	0.004	0.004
Cr_2O_3	0.00	b.d.		b.d.		0.59	0.35	0.08
MnO	0.00	b.d.		b.d.		0.27	0.28	0.03
Total	100	100.87		101.38		99.99	100.29	
Normative An, Di	$An_{36}Di_{64}$	$An_{43}Di_{57}$—$An_{47}Di_{53}$		$An_{40}Di_{60}$				
Glass density (g/l)				2782	26		3102	74

Table 1. Compositions of AD and LG experimental glasses. FeO* is all Fe calculated as FeO. The target composition for AD was the 1-atm eutectic composition on the anorthite-diopside binary (~$An_{36}Di_{64}$). The target composition for LG was Apollo 15 'yellow glass' and is based on composition #13 in Table 3 of Delano (1986). The target LG composition listed here has been modified from the original yellow glass composition reported by Delano (1986) by removal of 0.45 wt% Na_2O and renormalization to 100 wt%. Compositions were measured using a JEOL JXA-8200 electron microprobe with an accelerating voltage of 15 kV, a beam current of 10 nA, a beam diameter of ~10 µm and counting times of 20 s on-peak and 10 s on high and low backgrounds. Standards used for the electron microprobe analyses were Shankland forsterite (MgO); VG2 basalt glass (SiO_2); synthetic TiO_2 (TiO_2); synthetic anorthite (Al_2O_3, CaO); synthetic Cr_2O_3 (Cr_2O_3); synthetic fayalite (FeO); synthetic tephroite (MnO); Amelia albite (Na_2O); and Asbestos microcline (K_2O). Data were reduced using a modified ZAF procedure (Armstrong 1988). The composition listed for AD Batch 1 is an average of 10 analyses of two separate glass chips. These analyses revealed some compositional variability in AD Batch 1, which is reflected in the high standard deviation of analyses of this glass and the range of normative anorthite and diopside contents. The

composition listed for AD Batch 3 is the average of 10 analyses of two separate glass chips. The composition listed for LG is the average of four analyses of experiment LG3 and four analyses of experiment LG5. Analyses of a subset of our AD and LG run product glasses are provided in the supplement. Glass densities were measured for a few representative chips of our experimental glasses: the density reported for LG is an average of densities obtained for two LG3 glass chips and two LG4 glass chips, and the density reported for AD is an average of densities obtained for four chips of AD Batch 3 starting material; 1σ values are one standard deviation of these measurements.

Experiment	*Loop material*	*Batch (AD)*	*Duration*	*log(fO_2)*	ΔIW	*R*	pH_2 *(atm)*	pH_2O *(atm)*	pH_2/pH_2O	H_2O *(ppm)*	$^{16}O^1H/^{18}O$ *(SIMS)*
AD1b	Pt	1	2h58m	-8.79	1.12	0.48	0.06	0.27	0.22	402 (5)	
AD2	Pt	1	16h20m	-10.63	-0.72	2.36	0.45	0.25	1.79	383 (4)	0.068 (2)
AD3b	Pt	1	18h51m	-9.55	0.36	0.93	0.16	0.32	0.52	389 (6)	
AD5	Pt	1	16h05m	-8.00	1.91	0.23	1.47E-02	0.17	0.09	317 (5)	0.055 (1)
AD6	Pt	1	4h16m	-6.22	3.69	0.03	3.58E-04	0.03	0.01	146 (2)	
AD7	Pt	1	14h55m	-6.84	3.07	0.07	1.40E-03	0.06	0.02	199 (4)	
AD9	Pt	1	16h30m	-11.27	-1.35	4.33	0.64	0.17	3.71	268 (9)	0.048 (1)
AD10	Pt	1	18h57m	-9.49	0.42	0.88	0.15	0.32	0.48	376 (62)	0.073 (5)
AD11	Pt	1	17h28m	-12.23	-2.32	11.97	0.85	0.07	11.31	193 (8)	0.033 (1)
AD12	Pt	1	18h08m	-9.85	0.06	1.19	0.23	0.32	0.73	404 (6)	
AD13	Pt	1	18h42m	-8.68	1.23	0.44	0.05	0.26	0.19	397 (4)	
AD23	Pt	3	20h00m	-5.15	4.76	9.9E-03	3.2E-05	9.8E-03	3.3E-03	90 (11)	0.014 (1)
AD25	Pt	3	15h00m	-9.65	0.26	1.01	0.18	0.32	0.58	425 (5)	
AD26	Pt	3	21h14m	-11.92	-2.01	8.56	0.79	0.10	7.91	229 (2)	
LG1	Re		21h17m	-11.12	-1.20	3.73	0.60	0.19	3.12	269 (7)	
LG2	Re		16h16m	-10.50	-0.58	2.08	0.41	0.27	1.53	337 (9)	
LG3	Re		16h18m	-8.41	1.50	0.34	0.03	0.22	0.14	314 (13)	0.110 (3)
LG4	Re		46h53m	-8.83	1.08	0.50	0.06	0.27	0.22	370 (12)	
LG5	Re		Unknown	-6.94	2.97	0.07	1.7E-03	0.07	0.03	184 (53)	0.067 (1)
LG6	Mo		4h40m	-12.16	-2.25	11.03	0.84	0.08	10.38	186 (5)	
LG7	Mo		4h16m	-12.88	-2.97	24.46	0.92	0.04	23.79	143 (3)	0.0298 (3)
LG35	Pt		20h00m	-5.15	4.76	9.9E-03	3.2E-05	9.8E-03	3.3E-03	69 (3)	0.0231 (5)
LG38	Re		22h25m	-10.99	-1.08	3.31	0.56	0.21	2.71	323 (8)	0.091 (4)
LG39	Re		15h00m	-9.65	0.26	1.01	0.18	0.32	0.58	414 (12)	0.122 (3)
LG40	Re		21h14m	-11.92	-2.01	8.56	0.79	0.10	7.91	225 (6)	0.058 (1)

Table 2. Run conditions and results. All experiments were conducted at 1350 °C and 1 atm. Experimental durations are listed in terms of hours and minutes (e.g., 4h40m indicates a duration of 4 hours and 40 minutes). The experimental duration of LG5 is unknown because the Re loop underwent catastrophic volatilization and the experiment autoquenched. ΔIW is the difference between the oxygen fugacity of the experiment and the oxygen fugacity of the iron-wüstite buffer (calculated in log units). *R* is the ratio of mole fractions of H_2 and CO_2 in the introduced gas mixture (see Fig. 3). pH_2 and pH_2O are the partial pressures of hydrogen and water respectively, as calculated based on the measured fO_2 of the gas mixture (Deines et al. 1974). Water concentrations were measured by FTIR. 1σ errors of these measurements are listed in parentheses in terms of the least number of units cited (e.g., 402 (5) = 402 ± 5 ppm); these errors were estimated using a Monte Carlo approach, accounting for measurement errors in sample thickness, glass density, and peak height of the 3550 cm^{-1} peak in the FTIR spectra. For a subset of samples, $^{16}O^{1}H/^{18}O$ was measured using SIMS (see Fig. 6). 1σ errors are listed in parentheses in terms of the least number of units cited; errors were calculated as the standard deviation of multiple measurements (n=3–14 for AD and n=5–7 for LG).

FIGURE CAPTIONS

Figure 1 Concentrations of water dissolved as hydroxyl groups and as molecular water in melts vs. the total amount of dissolved water at low total water concentrations. Curves were generated using VolatileCalc (Newman and Lowenstern 2002), which adopts the regular solution model of Silver and Stolper (1989). The shaded region indicates the range of water concentrations measured in lunar olivine-hosted melt inclusions and glasses (Saal et al. 2008; Hauri et al. 2011; Saal et al. 2013; Chen et al. 2015; Wetzel et al. 2015). The water concentration range considered in this study is also indicated. The dominant dissolved species is expected to be hydroxyl at the total water contents relevant to our experiments and to lunar magmas.

Figure 2 Post-run concentrations of FeO* (all Fe as FeO) in a subset of our LG experiments run under a range of oxygen fugacities. Gray vertical dashed lines represent buffers (IW = iron-wüstite; QFM = quartz-fayalite-magnetite; NNO = nickel-nickel oxide; Re-ReO_2 = rhenium-rhenium oxide), calculated using expressions given by O'Neill and Pownceby (1993), O'Neill (1987), and Pownceby and O'Neill (1994). The horizontal orange line indicates the concentration of FeO* in the target Apollo 15 yellow glass composition (see Table 1). LG6 (not shown) and LG7 used molybdenum wire; LG35 (the most oxidizing experiment) used platinum wire; the remaining experiments represented in this figure were conducted using rhenium wire (see Table 2 for further details of run conditions). Full analyses of the run products shown in this figure are provided in the supplement.

Figure 3 Partial pressures of H_2, CO_2, and H_2O in vapor as functions of log(fO_2) at 1350°C and P_{tot}=1 atm. Top axis: R is the ratio of mole fractions of H_2 and CO_2 in the introduced gas mixture. Gray vertical lines are buffers (IW = iron-wüstite; QFM = quartz-fayalite-magnetite; see references in Fig. 2).

Figure 4 (a) Full spectra of LG and AD glasses at 1500–6000 cm^{-1}. Peak positions assigned to various H-O species (Stolper 1982b) are indicated by vertical gray dashed lines and labeled along the top axis. The 3550 cm^{-1} total water peak [labeled *OH (total)*] is clearly visible in all spectra. Note the lack of molecular water peaks at 5200 cm^{-1} (labeled H_2O_{mol}) and at 1630 cm^{-1} [the molecular water fundamental vibration; labeled H_2O_{mol} *(f)*], and the lack of a hydrogen peak at ~4130 cm^{-1} (Hirschmann et al. 2012). In spectra of LG glasses, the 3550 cm^{-1} peak is superimposed on a broad sloping background of high absorbance due to the presence of large quantities of iron in this composition (Bell et al. 1976; Stolper 1982b). The region of high absorbance at wavenumbers less than ~2000 cm^{-1} is due to absorption by the silicate network. **(b)** Background-corrected spectra. These spectra were obtained by subtracting a linear background from the raw spectra. LG40 and AD26 were equilibrated in the furnace at the same time (i.e., at the same pH_2O and fO_2 conditions). LG35 contains the lowest measured water concentration of all the experiments (69 ppm total water); the 3550 cm^{-1} water peak is clearly resolved even at this low concentration. LG4 is one of the highest concentration experiments (370 ppm total water). Spectra have been vertically offset arbitrarily for clarity.

Figure 5 (a) Demonstration of a proportional relationship between the concentration of water in AD experimental glasses (measured by FTIR) and the square root of the partial pressure of water in the furnace atmosphere (calculated from the measured fO_2 in the furnace atmosphere using the free energy of reaction expressions from Deines et al. (1974) for H_2-CO_2 gas mixtures at 1 atm). The dashed line is a least-squares linear regression forced through the origin (equation (7)). Vertical error bars are 2σ and take into account measurement errors in peak height, density, and glass thickness. Horizontal error bars assume fO_2 measurement precision of 0.15 log units. All experiments at 1350 °C and 1 atm. **(b)** Same as (a) for the LG experimental glasses. Symbols and error bars as in (a). **(c)** Concentration of water in AD experimental glasses (measured by FTIR) vs. log(fO_2). The concentration data define a symmetric bell-shaped curve suggesting that the solubility of water in AD melts is independent of pH_2/pH_2O, which decreases monotonically from

low to high log(fO_2). The dashed blue curve is a translation of the best-fit line from (a) into log(fO_2) space, using the relationship between fO_2 and pH_2O given by Deines et al. (1974) for H_2-CO_2 gas mixtures at 1 atm. Symbols and error bars as in (a). Dashed gray vertical lines mark the positions of the iron-wüstite (IW), quartz-fayalite-magnetite (QFM), and nickel-nickel oxide (NNO) buffers; references in the caption to Fig. 2. **(d)** Same as (c) for the LG composition.

Figure 6 (a) Counts of $^{16}OH/^{18}O$ measured by SIMS versus concentration of water measured by FTIR in AD experimental glasses. SIMS data points represent the mean of 3–14 separate analyses of each experimental glass, made over the course of two analytical sessions. Filled symbols are experiments run under reducing conditions (fO_2<IW+0.3) and open symbols are experiments run under oxidizing conditions (fO_2>IW+0.3). Vertical error bars represent two standard deviations of 3–14 separate SIMS analyses; horizontal error bars are 2σ and take into account measurement errors in peak height, density, and glass thickness that enter into the FTIR analyses. For AD glasses, SIMS and FTIR data are proportional, even for the most reducing experiments, suggesting that all of the hydrogen in the melt is dissolved as hydroxyl and the dissolution of H_2 has not been detected. The least-squares linear regression of the data (blue dashed line) has a high R^2 value of 0.99, i.e., the proportional relationship between water concentration and $^{16}OH/^{18}O$ accounts for almost all of the variance in $^{16}OH/^{18}O$, thereby precluding a significant role for variable H_2 dissolution in these glasses. **(b)** Same as (a) for LG composition. For this composition, the oxidized experiments produce higher counts of $^{16}OH/^{18}O$ at a given FTIR-measured water concentration than the reduced experiments. This is the opposite of what would be expected if H_2 dissolution were contributing to the counts of $^{16}OH/^{18}O$, so instead this likely indicates the influence of melt structure and composition on the production and transport of secondary ions in the SIMS (i.e., the difference between the reduced and oxidized experiments may be a matrix effect related to differences in iron oxidation state and iron concentration in the melt in response to several orders of magnitude variability in fO_2). Symbols and error bars as in (a).

Figure 7 (a) Calculation to demonstrate the expected effect of H_2 dissolution on the relationship between dissolved H (as H_2O_{mol}+OH±H_2) and $^{16}OH/^{18}O$ measured by SIMS. FTIR measurements of water concentration, recalculated as ppm H and assuming no dissolved H_2, are shown as blue circles. Filled blue circles are experiments run under reducing conditions (fO_2<IW+0.3) and open blue circles are experiments run under oxidizing conditions (fO_2>IW+0.3). Black squares represent a model in which molecular hydrogen makes up a significant proportion of the total dissolved H in the melt. Dissolved H_2 is assumed to be proportional to pH_2 with a solubility of 10 ppm per bar of pH_2 [this high assumed solubility is for illustrative purposes only; a range of H_2 solubility is considered in (c)]. Note that the reduced (i.e., high pH_2) experiments are predicted to have elevated concentrations of H in this model (due to the addition of dissolved H_2; highlighted by vertical arrows) but the oxidized experiments experience little to no change in total H concentration. The addition of H_2 to the melt in proportion to the imposed pH_2 of each experiment (see Table 2) degrades the correlation between dissolved H and $^{16}OH/^{18}O$, resulting in a lower R^2 value and suggesting that H_2 dissolution is not significant under the conditions of our experiments. Horizontal error bars represent two standard deviations of replicate measurements. **(b)** Same as (a) for the LG composition. Our original FTIR and SIMS data are plotted as open (fO_2>IW+0.3) and filled (fO_2<IW+0.3) orange circles. Dissolved H_2 is assumed to be proportional to pH_2 with a solubility of 10 ppm per bar of pH_2. The addition of H as H_2 to the melt degrades the expected correlation between total H and $^{16}OH/^{18}O$ (measured by SIMS), suggesting that H_2 dissolution in our LG experiments is not significant. **(c)** Misfit ($1-R^2$) of the model described in (a) for a range of assumed H_2 solubilities from 0 to 10 ppm per bar of pure H_2. The addition of H as H_2 to the total H budget of our experimental AD melts degrades the correlation between calculated total H and $^{16}OH/^{18}O$ measured by SIMS, regardless of the assumed solubility of H_2, supporting a negligible role for H_2 dissolution in our experiments. **(d)** Same as (c) for the LG composition.

Figure 8 Comparison of data from this study with those from Baker and Grove (1985) and Dixon et al. (1995). Water solubility data from Baker and Grove (1985) for basaltic andesite melts equilibrated with H_2-H_2O and H_2/CO_2 gas mixtures at 1 atm and ~1200 °C are shown as black squares with red outlines. The Baker and Grove (1985) data points have been recalculated with ε_{3550}=63 l/mol-cm to be consistent with our treatment of AD and LG data. The accuracy of the Baker and Grove (1985) data is estimated to be 10 rel.% (error bars are smaller than the symbol size) based on the compilation of values of ε_{3550} by Shishkina et al. (2014) (see discussion in section 3.3). Water solubility data from Dixon et al. (1995) for MORB melts equilibrated at temperatures of ~1200 °C and pressures of 176 – 980 bar are shown as black filled circles (hydroxyl only) and gray diamonds (total water dissolved as both hydroxyl and molecular water). Error bars on the Dixon et al. (1995) data are 2σ. Our water solubility data for AD and LG melts at 1350 °C are consistent with the data of Baker and Grove (1985) supporting only a weak dependence of water solubility on melt composition and temperature. Extrapolations of our results to the conditions of the Dixon et al. experiments using equations (7) and (8) (orange and blue dashed lines) provide good matches to the concentrations of hydroxyl measured by Dixon et al. (1995) but project to lower concentrations than the total water content of these experiments (i.e., the sum of dissolved molecular water and hydroxyl). This behavior is as expected based on equations (1) and (4) (see discussion in section 5.1).

Figure 9 Comparison of data from this study with extrapolations to low pressures of published water solubility models. **(a)** Comparison between data of this study (orange circles are our LG experiments; blue circles are our AD experiments) and water solubility calculated using the VolatileCalc model of Newman and Lowenstern (2002) for basaltic melts at 1350 °C containing 43 wt% SiO_2 (orange dashed curve; closely corresponding to the LG composition with 43.6 wt% SiO_2) and 49 wt% SiO_2 (blue dashed curve; corresponding to the AD composition with ~50 wt% SiO_2). **(b)** Comparison between data collected during this study (blue and orange circles) and the composition-dependent water solubility model of Moore et al. (1998) (dashed colored curves). **(c)** Comparison between data collected during this study (blue and orange circles) and the composition-dependent mixed-volatile solubility model of Papale et al. (2006) (dashed colored curves). Model curves were generated using the online calculator at http://ctserver.ofm-research.org/Papale/Papale.php. **(d)** Comparison between data from this study (blue and orange circles) and the composition-dependent water solubility model of Iacono-Marziano et al. (2012).

Figure 10 (a) Partial pressures of H_2O, H_2, CO_2, and CO in equilibrium with a lunar melt containing 14.5 ppm dissolved H_2O and 0.36 ppm dissolved C (e.g., the composition measured 20 μm from the surface of glass bead D20 by Wetzel et al. 2015). Assumptions of these calculations and models for C speciation and solubility are discussed in section 5.2. Note that the partial pressures of H_2O (0.0005 bar) and H_2 (0.0011 bar) are too small to be visible. **(b)** Partial pressures of H_2O, H_2, CO_2, and CO in equilibrium with a lunar melt containing 1200 ppm dissolved H_2O and 4 ppm dissolved C (e.g., the composition of lunar melt inclusions characterized by Wetzel et al. 2015). See section 5.2 for a detailed description of these calculations.

Figure 11 (a) Concentrations of water and carbon measured in lunar olivine-hosted melt inclusions (Hauri et al. 2011; Wetzel et al. 2015; shown as orange diamonds) and pyroclastic glass beads (Saal et al. 2008 and Wetzel et al. 2015; shown as white diamonds). All melt inclusion compositions are corrected for post-entrapment crystallization (Wetzel et al. 2015). Also shown are batch degassing calculations for a magma initially containing 4 ppm C and 1200 ppm H_2O (red curve) and for a magma initially containing 64 ppm C and 1200 ppm H_2O (black curve). Labeled tick marks on the black curve indicate saturation pressures (in bar) of the corresponding melt compositions. A detailed description of these calculations is provided in section 5.4. **(b)** Calculation of the relationship between vapor volume percent and total pressure for batch degassing of a magma initially containing 64 ppm C and 1200 ppm H_2O (black curve), and a magma initially containing 4 ppm C and 1200 ppm H_2O (red curve). The vapor is assumed

to behave as an ideal mixture of ideal gases, and we assume that oxygen fugacity is defined by IW−1. The melt is assumed to have a density of 3000 kg/m^3 (e.g., Rutherford and Papale 2009). We apply a simple vapor volume fraction fragmentation criterion of ~65–75 vol. % (e.g., Spera 1992; Gonnermann and Manga 2012) to show that both magma compositions would be expected to fragment at a pressure of ~5 bar (corresponding to a depth beneath the lunar surface of ~120 m). **(c)** Variation of partial pressures of H_2O, H_2, CO_2, and CO with total pressure in vapor exsolved during batch degassing of a magma initially containing 64 ppm C and 1200 ppm H_2O. At pressures >~15 bar, the vapor composition is dominated by CO. **(d)** Same as **(c)** for total pressures <50 bar. At total pressures <~15 bar, the vapor composition changes from being CO-dominated to being H_2-dominated. At the estimated fragmentation pressure of ~5 bar (indicated by the vertical dashed line) the vapor is H_2-dominated. **(e)** Variation of volume percentages of H_2O, H_2, CO_2, and CO with total pressure in vapor exsolved during batch degassing of a magma initially containing 64 ppm C and 1200 ppm H_2O. At pressures >~15 bar, the vapor composition is dominated by CO. **(f)** Same as **(e)** for total pressures <50 bar. At the estimated fragmentation pressure of ~5 bar (indicated by the vertical dashed line) the vapor is H_2-dominated, suggesting that H_2 was the primary propellant of the lunar fire fountain eruptions. See discussion in section 5.4.

Figure 1

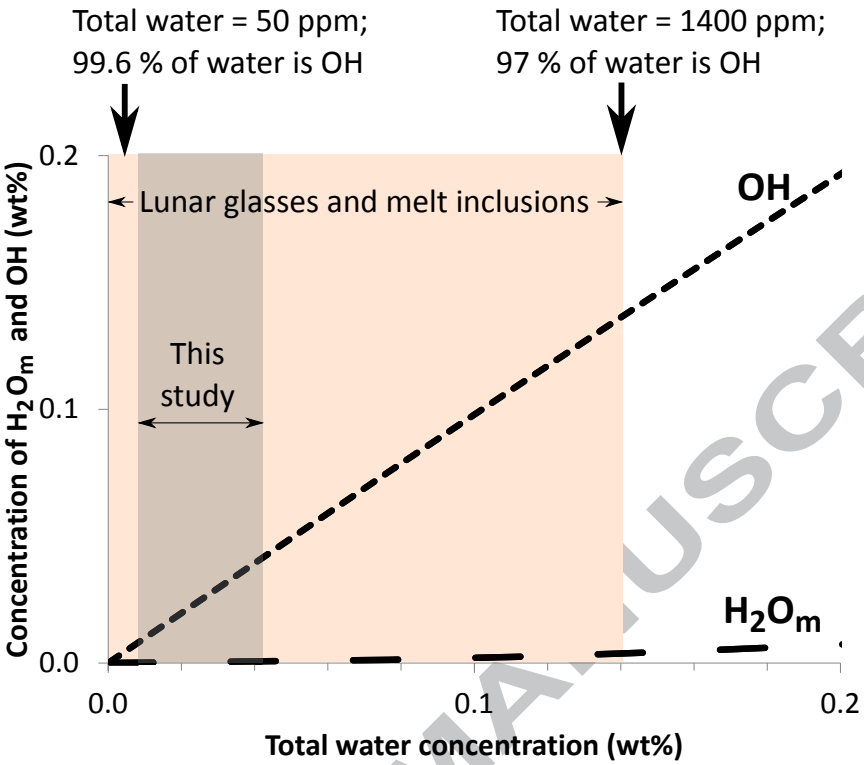

Figure 2

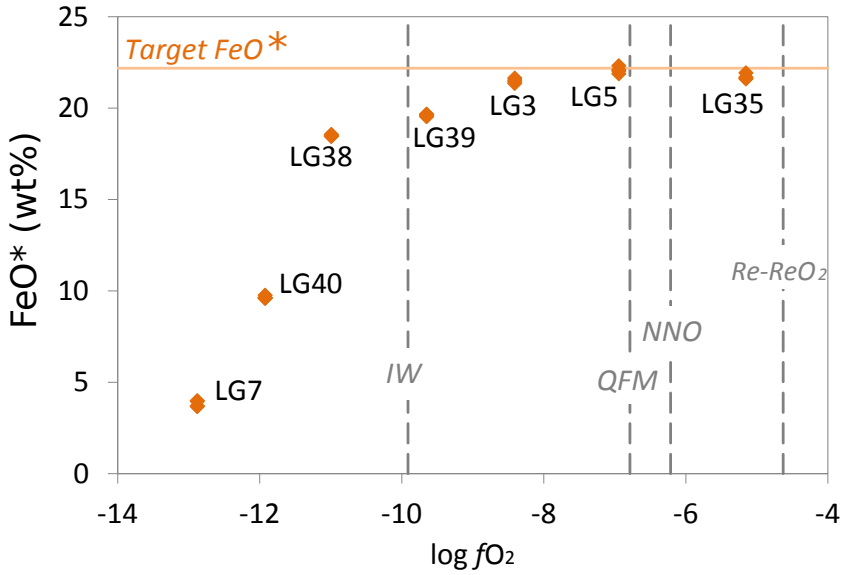

Figure 3

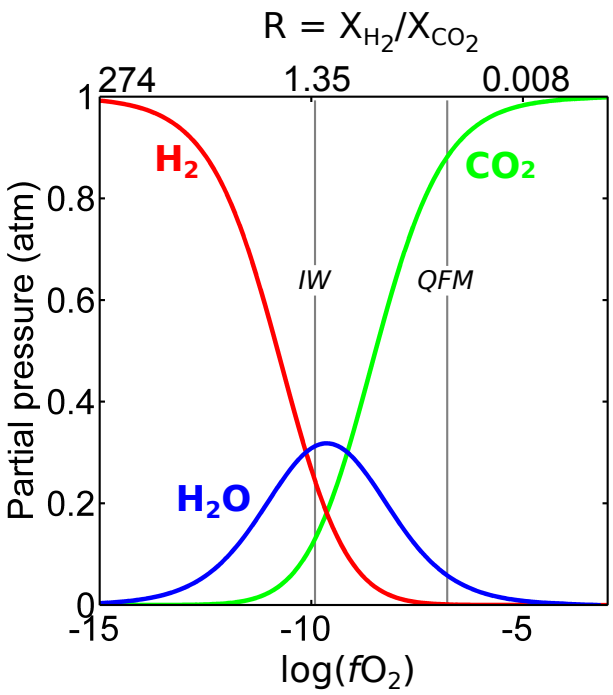

Figure 4

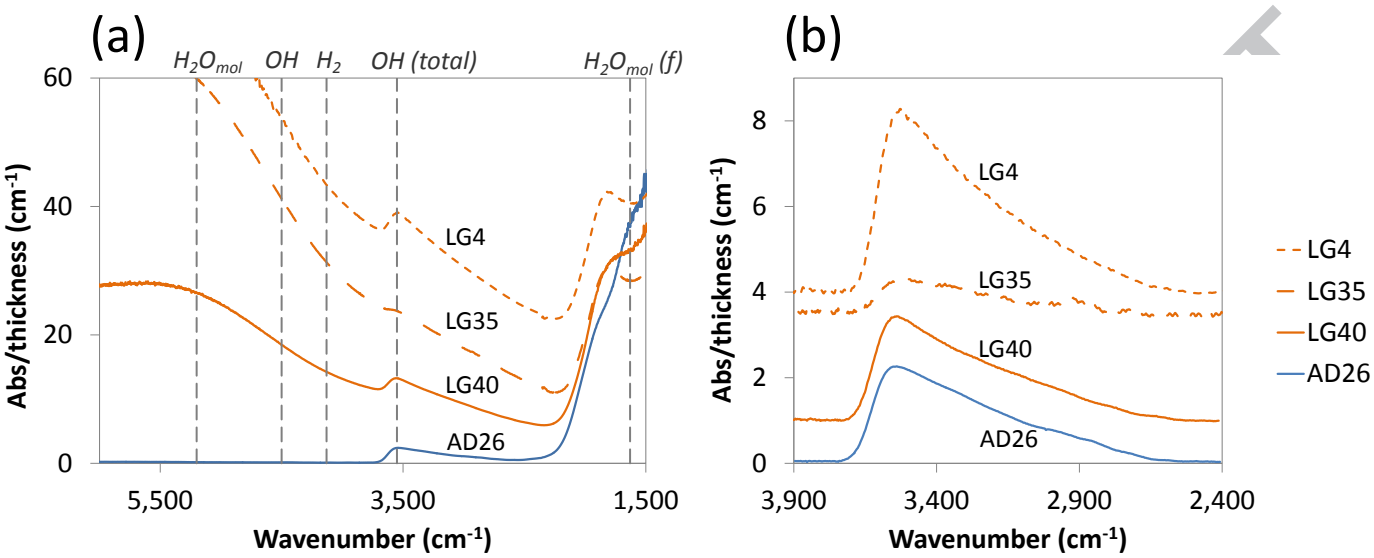

Figure 5

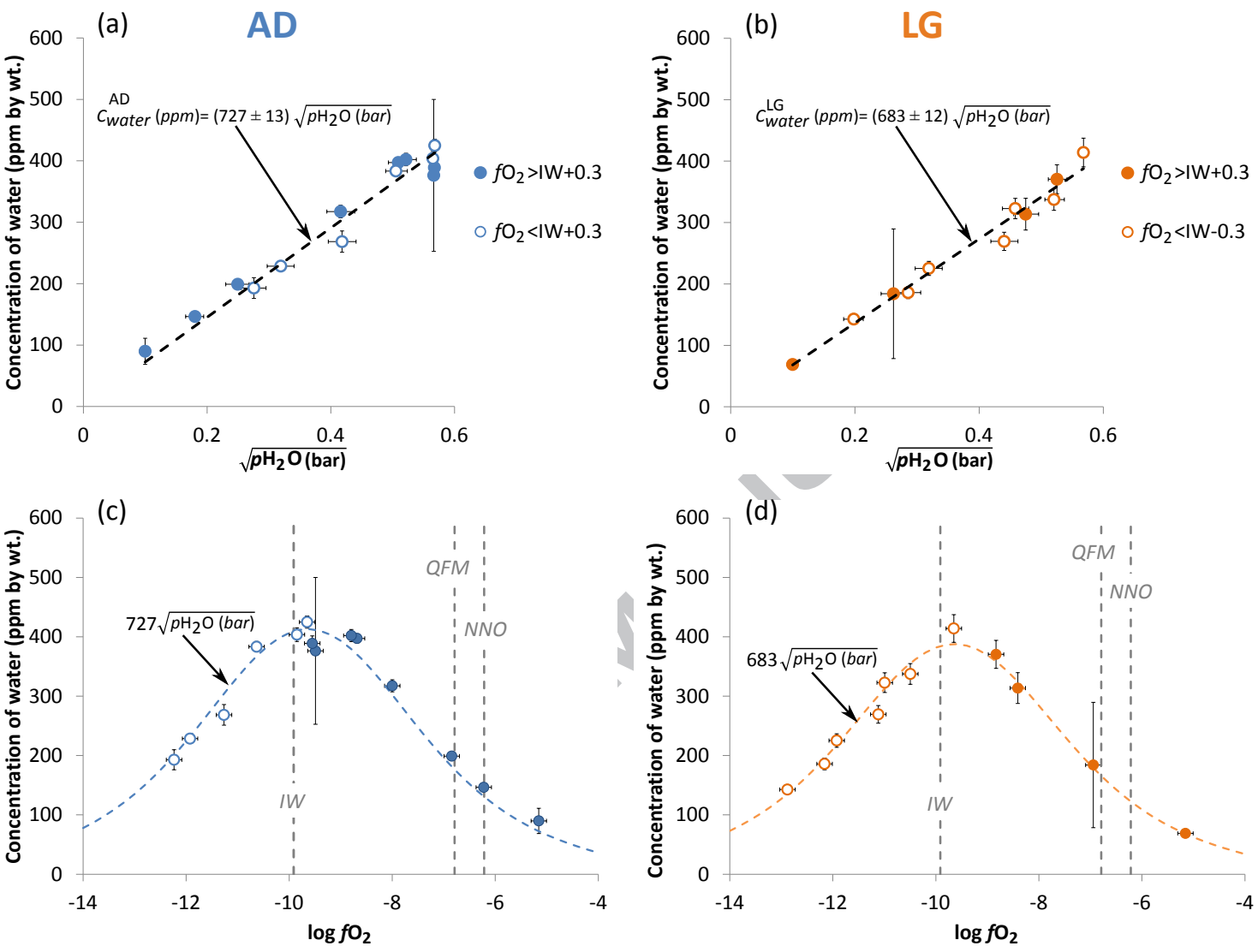

Figure 6

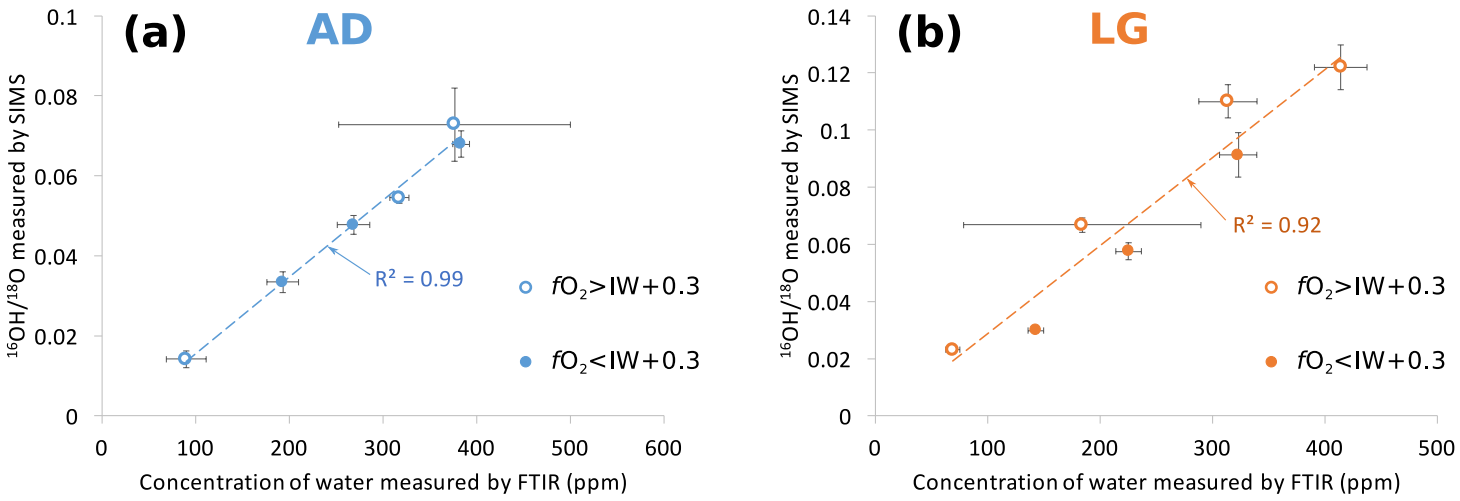

Figure 7

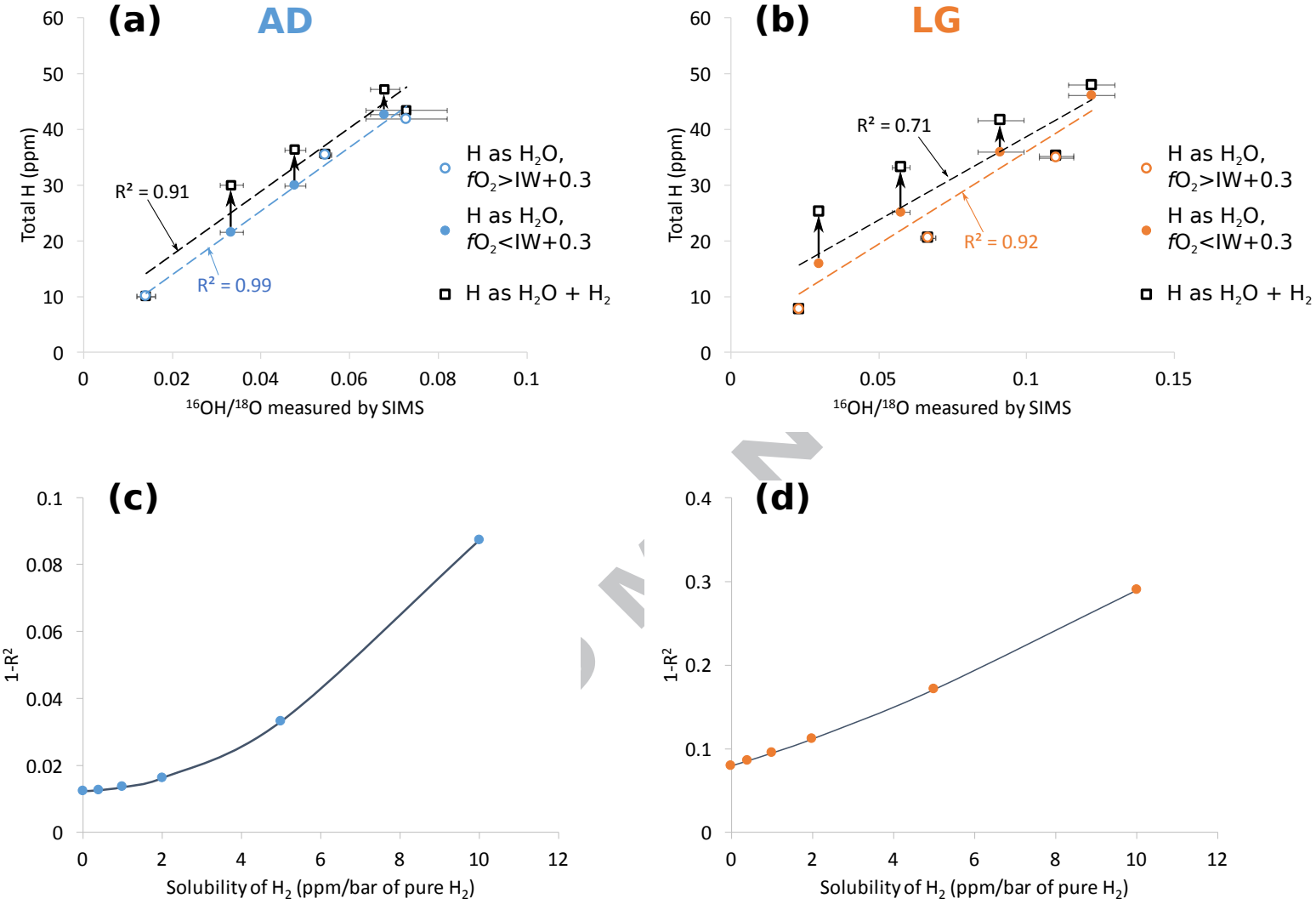

Figure 8

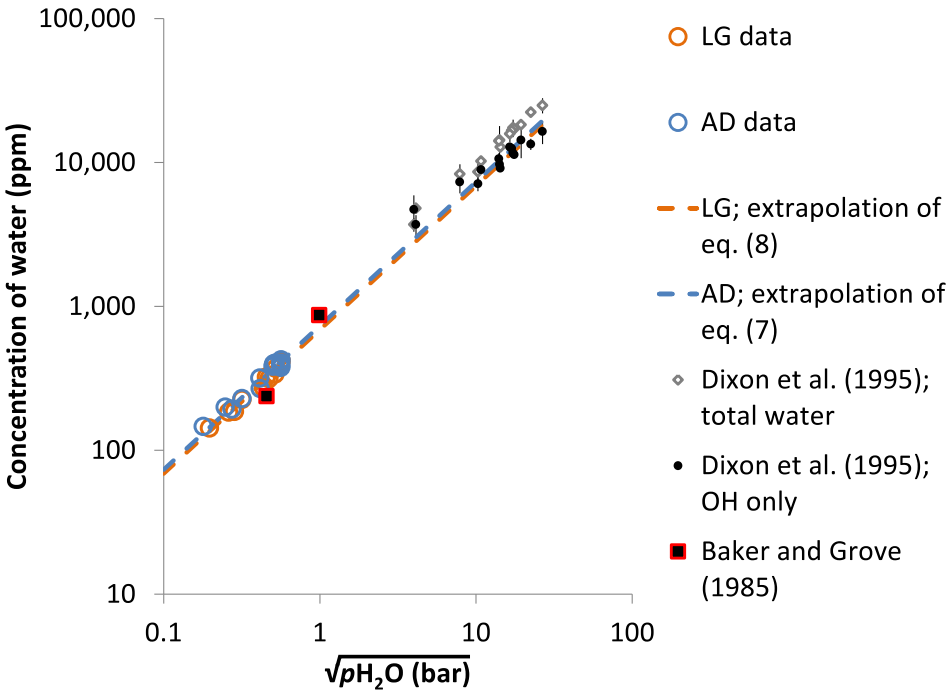

Figure 9

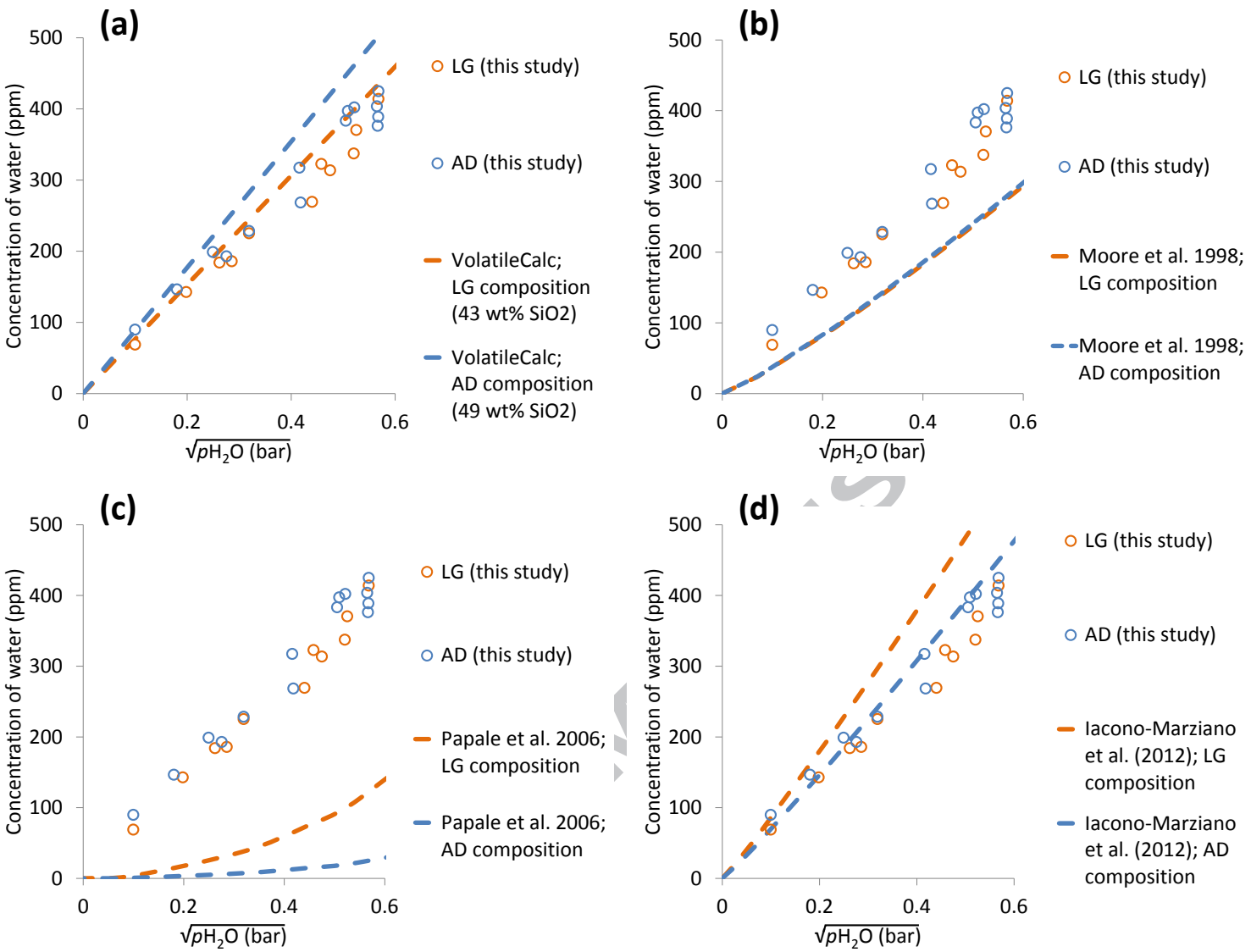

Figure 10

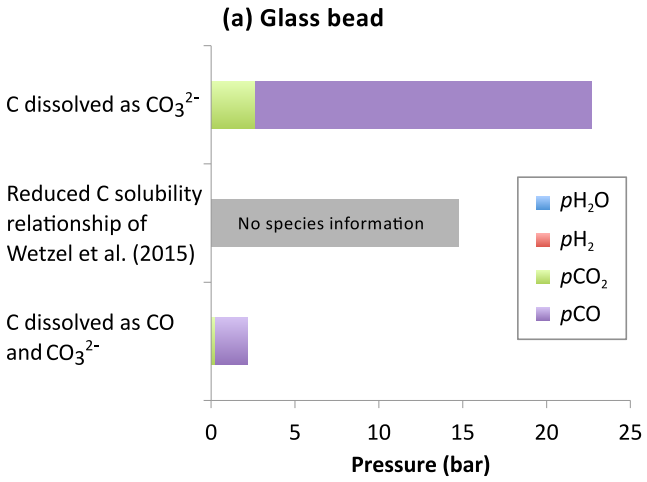

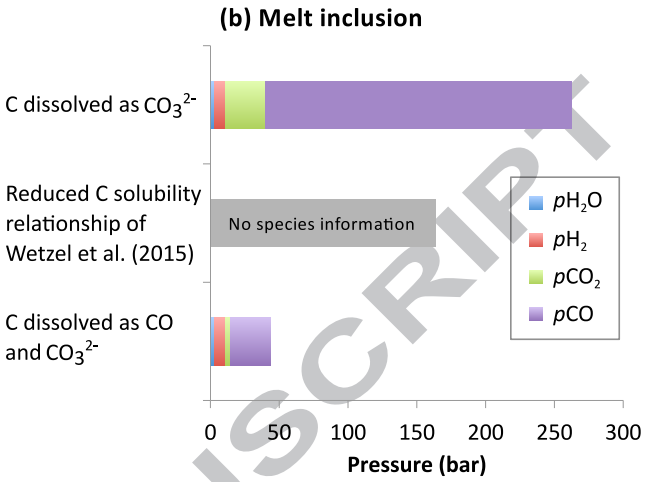

Figure 11